
Unterschrift Betreuer



DIPLOMARBEIT

Tumor motion trajectory estimation to compensate for monitoring latency when using real-time 2D/3D registration

ausgeführt am Atominstitut (E 141)
der Technischen Universität Wien

in Zusammenarbeit mit dem

Universitätsklinik für Strahlentherapie
der Medizinischen Universität Wien

unter der Anleitung von

Univ.-Prof. DI Dr. Dietmar Georg

(Medizinische Universität Wien)

Hugo Furtado, PhD.

(Medizinische Universität Wien)

durch

Paul Semmelrock, BSc.

Simon-Denk-Gasse 2
A-1090 Wien

Wien, March 22, 2018

Ort, Datum

Unterschrift Student

Abstract

During radiotherapy treatments of thoracic and abdominal tumors, tumor motion due to respiration has to be considered. Tracking based delivery systems can follow the tumor in real time and therefore enable more precise treatments. One of the problems of such systems is that monitoring the tumor and then reacting to its movement takes a certain amount of time i.e. there is an overall system latency. In this thesis, approaches to cope with system latencies are investigated. Two approaches are considered: a) correlation between external and internal motion, as external observations can be made with virtually no latency and b) motion prediction where a position estimate in the future can be derived from past observations. In systems with very high latencies, comprised of x-ray imaging latencies and response latencies of the beam positioning system, both external-internal correlation as well as prediction has to be integrated. The external-internal correlation models of two commercially available systems, the MHI vero4DRT and the Cyberknife®/Synchrony™ system, were investigated and compared to each other. A predictor was implemented based on Extended Kalman Filtering with a local dynamic model, which is motivated by the elliptic shape of respiratory motion in a plane augmented with time-delayed axes. The prediction and correlation methods were combined in a C++ algorithm. The algorithm performance was evaluated on corresponding tumor and chest motion traces measured on 8 patients at the Mitsubishi RTRT in combination with the AZ 733V Anzai medical belt. The data was simulated for a realistic choice of system parameters, hence 2s imaging- and 100ms beam positioning latency. It was shown that the average root-mean-squared-error of the estimated tumor position over all patients is $\sim 1.25\text{mm}$ for an average $\sim 12.3\text{mm}$ tumor motion amplitude. The developed algorithm is not capable of compensating circular tumor movement, which results in slightly higher errors in patients showing such characteristics. As an extension of this project, it would be interesting to include circular motion compensation in the algorithm.

Contents

1	Introduction	1
1.1	External Beam Radiotherapy	1
1.1.1	Linear Accelerator	1
1.1.2	Volumes and Margins in Radiotherapy	3
1.1.3	Treatment Planning and Dose Calculation	5
1.1.4	Treatment Techniques	6
1.1.5	Inter- & Intra-fraction Motion Compensation	7
1.2	Respiratory Motion Management	10
1.2.1	Abdominal Compression	10
1.2.2	Breath-Hold Methods	11
1.2.3	Respiratory Gating	11
1.2.4	Real-Time Tumor Tracking	12
1.3	Identification of the Tumor	14
1.3.1	Tumor Localization Methods	14
1.3.2	Localization Tools	16
1.3.3	Correlation Models	21
1.4	Anticipating the Tumor Motion	27
1.4.1	Model-based Prediction	27
1.4.2	Model-free Prediction	29
1.5	Motivation	32
2	Methods	33
2.1	Cyberknife [®] Synchrony [™] Correlation Method	33
2.2	MHI vero4DRT Correlation Method	37
2.3	Local Circular Motion Model	37
2.4	Developed Algorithm	42
2.4.1	Armadillo Linear Algebra Library	42

2.4.2	Conceptual Workflow	42
2.4.3	Decision Tree	43
3	Results	49
3.1	Updating efficiency	50
3.2	Prediction Potentials and Limits	51
3.3	Algorithm Performance	54
4	Discussion and Conclusion	57
	Acknowledgments	61
	Bibliography	63

Chapter 1

Introduction

In 2015, 39.906 new cases of cancer were documented in Austria, 21.252 in men and 18.654 in women. In 2015, cancer killed 10.865 men and 9.344 women. Thus, they account for about a quarter of annual deaths [1].

Commonly used treatment techniques are chemotherapy, surgery and radiotherapy. Radiotherapy itself can be divided into brachytherapy (internal radiotherapy), in which a sealed radioactive source is placed within or in the immediate vicinity of the volume to be irradiated in the body, and external beam radiotherapy (EBRT), where high-energy photon- or particle beams are generated with a particle accelerator and aimed at the part of the patient's body where the tumor is located. The latter will be described in more detail in this chapter.

1.1 External Beam Radiotherapy

1.1.1 Linear Accelerator

The main delivery system for generating high energy photon and electron beams are linear accelerators (LINAC). In LINACs electrons are produced by an electron gun and are accelerated to high energies using radiofrequency waves. The electrons are stopped by a target and thereby produce x-rays. The x-ray profile is collimated before it is used to treat patients. For e^- therapy the e^- pencil beam is scattered with foils to obtain clinical field sizes of up to $20 \times 20\text{cm}^2$.

1.1.1.1 Production and Acceleration of the e^- -Beam

Electrons are emitted from a cathode, using thermionic emission, and are accelerated to an anode by a constant electrical potential difference U_B . The kinetic energy of the accelerated electron is given by $E_k = eU_B$. The beam leaves the electron gun through a hole in the anode and enters the accelerating structure.

The acceleration structure is needed to further accelerate the electrons, since the achievable energy of the electron gun is limited to the kilovoltage region. The acceleration of any charged particle can be performed either by using a travelling- or standing waveguide. A waveguide consists of a hollow tube, separated by copper plates with a hole in its center. The separate departments of the tube are then charged using either a standing wave, where the acceleration depends on wave's frequency or a travelling wave, where the phase velocity governs the acceleration.

1.1.1.2 Production of Photon Beams

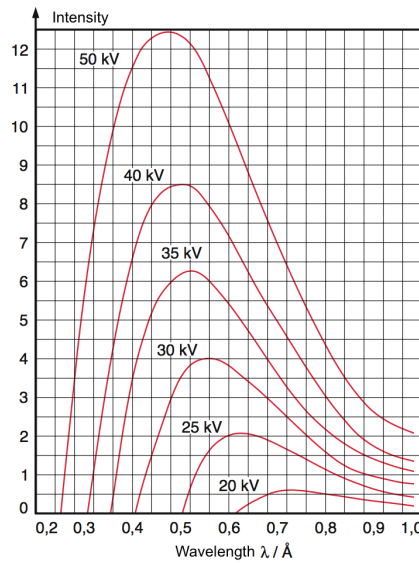


Figure 1.1: Energy spectrum of Bremsstrahlung for different electron energies (image from [2])

When the high energy electron beam hits the target, it interacts with the nuclei of the target atoms. The negatively charged electron is scattered at positively charged nuclei and changes its path. This corresponds to accelerated charge, which leads to the emission of electromagnetic radiation called Bremsstrahlung. The energy of the Bremsstrahlung equals the loss of kinetic energy of the electron. The closer the

electron gets to the nucleus during the scattering process, the more energy it loses. The probabilistic character of this scattering process leads to the Bremsstrahlung having a continuous spectrum of energy (fig. 1.1). Beam flattening filters are then used to improve the homogeneity of the x-ray beam.

1.1.1.3 Beam collimation

A beam collimator is used to shape the x-ray beam. This can either mean that the beam becomes more aligned in one direction or that the beam's cross section is reduced. Most linear accelerators use multiple collimators. A primary collimator is used to align the beam, hence reduce the maximum angle of the exiting beam. A second collimator consists of lead blocks and is used to restrict the beam to a coarse, rectangular shape. An additional collimator with separate lead leaves that can move independently can be placed after the second collimator. This so called Multi-leaf Collimator (MLC) can be used to form a desired field shape e.g. to fit the tumor shape in 2D. The schematic structure of an MLC is shown in figure 1.2.

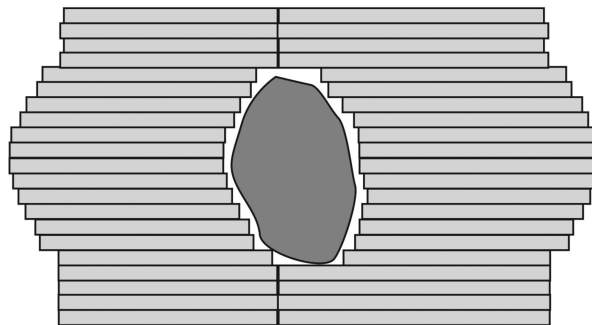


Figure 1.2: Multileaf collimeter used to form the beam (image from [?])

1.1.2 Volumes and Margins in Radiotherapy

The goal of EBRT is to kill malignant cancer cells by destroying their ability to reproduce, while the dose to neighbouring healthy tissue needs to be as low as possible. This means that the therapeutic window needs to be optimized, by simultaneously improving the Tumor Control Probability (TCP) and the Normal Tissue Control Probability (NTCP). However, it is not possible to treat tumors without irradiating neighbouring healthy tissue. Therefore, a number of different tumor volumes and margin concepts were introduced in order to standardize the description and analysis of the distributed dose.

In this section we will briefly describe the volume and margin concepts, that are illustrated in fig. 1.3. Detailed descriptions are given in the ICRU report 50 and 62 [3, 4].

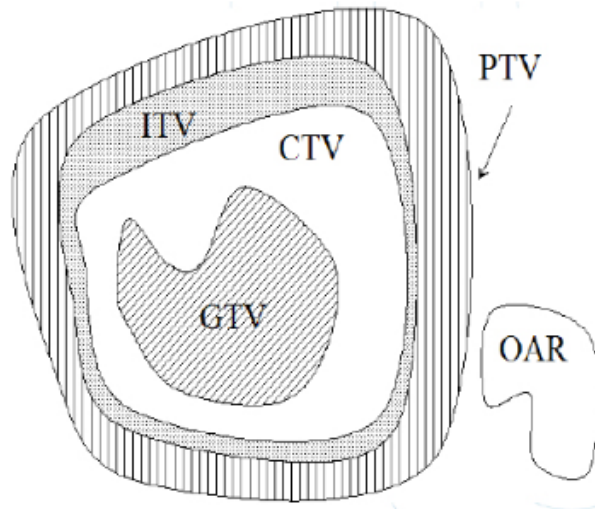


Figure 1.3: Illustration of volume concepts in radiotherapy as defined in the ICRU reports 50 and 62 [3, 4] (image from [5])

- **GTV** Gross Tumor Volume: *"is the gross palpable or visible/demonstrable extent and location of malignant growth"* [3].
- **CTV** Clinical Target Volume: *"is the tissue volume that contains a demonstrable GTV and/or subclinical microscopic malignant disease, which has to be eliminated. This volume thus has to be treated adequately in order to achieve the aim of therapy, cure or palliation"* [3].
- **IM** Internal Margin: *"is defined so as to take into account variations in size, shape, and position of the CTV in relation to anatomical reference points (e.g. filling of stomach, bladder, movements due to respiration, etc.)"* [4].
- **ITV** Internal Target Volume: *"is defined as the sum of Clinical Target Volume (CTV) and Internal Margin (IM)"* [4].
- **SM** Setup Margin: *"takes into account all uncertainties in patient-beam positioning"* [4].

- **PTV** Planning Target Volume: *"is a geometrical concept, and it is defined to select appropriate beam size and beam arrangements, taking into consideration the net effect off all possible geometrical variations and inaccuracies in order to ensure that the prescribed dose is actually absorbed in the CTV"* [3]. In ICRU 62 [4] the PTV was redefined as the sum of the SM and ITV.
- **OR** Organ at Risk: *"are normal tissues whose radiation sensitivity may significantly influence treatment planning and/or prescribed dose"* [3,4].
- **PRV** Planning Organ at Risk Volume: *"is a geometrical concept, and it is defined in the same way as the PTV for the CTV, taking into consideration the net effect off all possible geometrical variations (movements and changes in shape) of the OR as well as set-up uncertainties when considering radiation effects on the OR"* [3,4].

1.1.3 Treatment Planning and Dose Calculation

At the beginning of a radiotherapy treatment, a 3D model of the patient is created. This is typically done with a CT scan or magnetic resonance imaging for better soft tissue contrast. The 3D model is used by the planner or a physician to define the volumes and margins, that were described above.

Based on the these volumes the treatment parameters, such as the dose level, the number of beams and the angle of incidence, are chosen by the planner. Dose calculation then present the link between the treatment parameters defined in the planning process and their clinical outcome. The primary physical quantity used to analyse the effect of the treatment, is the distribution of absorbed dose. The treatment parameters need to be optimized in order that 95% of the PTV receive 95% of the prescribed dose. Additionally, multiple constraints such as the Median Dose ($D_{50\%}$), Near-min Dose ($D_{98\%}$), and the Near-max Dose ($D_{2\%}$) to different volumes are defined, which make the optimization process challenging [6,7]. Treatment planning is an iterative process, that ends with the optimized treatment plan.

In order to implement this elaborate treatment plan, the positioning of the patient at the beginning of the irradiation must be accurate and should not change during the irradiation. We discuss this problem in more detail in the following sections.

1.1.4 Treatment Techniques

EBRT techniques have been improved significantly over the past few decades. It started out as a 2D technique. Conventional radiotherapy uses 2D rectangular treatment fields. However, a tumor is usually irregular-shaped. This leads to a great amount of normal tissue being irradiated. With the introduction of computed tomography (CT) treatment plans were expanded to three dimensions, which lead to the introduction of conformal radiotherapy (CFRT). CFRT can be divided into two main groups: (1) **3D-conformal radiotherapy**, which only uses geometrical field shaping and (2) **intensity-modulated radiotherapy (IMRT)**.

1.1.4.1 3D Conformal Radiotherapy

3D conformal radiotherapy shapes the beam to the PTV. To reduce the high dose region the number of beams is usually greater than in standard RT techniques. It only uses geometrical field shaping, which only allows for the treatment of tumor volumes with convex surface shapes. The treatment of tumor volumes with concave surfaces would overdose healthy tissue or even OAR in the concavity.

Successful 3D conformal radiotherapy relies on the interplay of several steps in the so called "patient-treatment-chain", consisting of the 3D target localization, 3D treatment planning and 3D dose delivery.

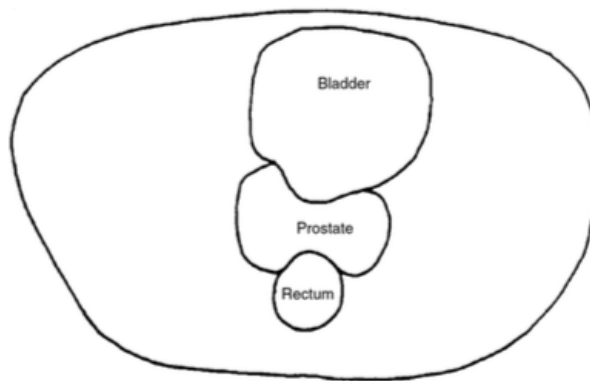


Figure 1.4: The need for IMRT in the case of a concave tumor shape exemplified by the prostate. Both bladder and rectum classify as OAR. [8]

1.1.4.2 Intensity Modulated Radiotherapy (IMRT)

With Intensity Modulated Radiotherapy (IMRT) it became possible to modify not only the beam shape but also the intensity of the beam during treatment. The aim

of IMRT is to deliver higher dose to the target and ensure better OAR sparing. The treatment field is subdivided in smaller sub-fields with a uniform photon fluence, which can be varied independently. The beam angle with respect to the patient is changed several times during treatment. Therefore, a reduced sub-field intensity from one direction, e.g. in order to spare an OAR, can be compensated by a higher sub-field intensity from another direction. Thus, it allows for treating tumor volumes with a convex shape (fig. 1.4).

An advancement of IMRT is the Volumetric Intensity Modulated Arc Therapy (VMAT). In VMAT the radiation is delivered by a LINAC that is rotated around the patient. Both rotational speed and intensity can be modulated. The field shape is continuously adjusted by an MLC. This allows for a high degree of flexibility during treatment. Therefore the total application time is considerably shorter than with the IMRT.

1.1.5 Inter- & Intra-fraction Motion Compensation

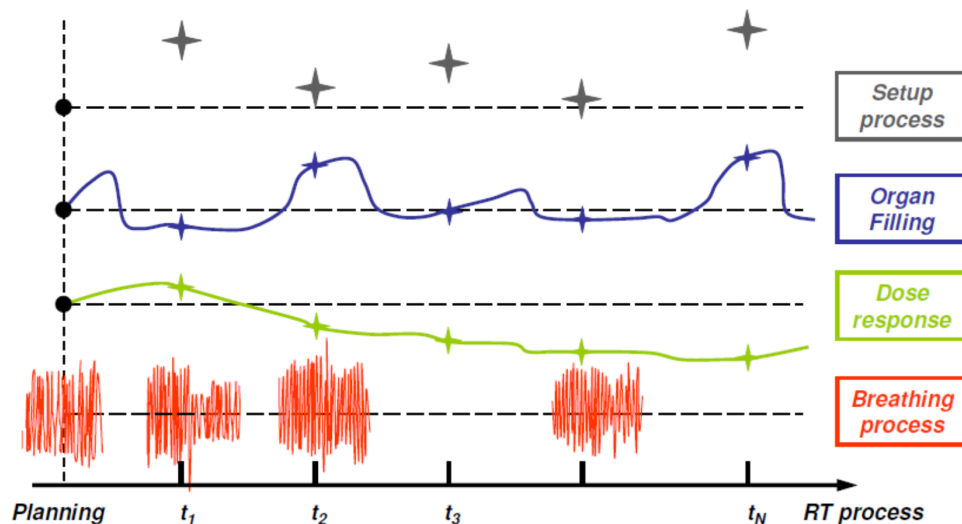


Figure 1.5: 4D effects of intra- and interfraction motion on treatment uncertainties: showing the error of the setup process (grey), due to organ filling (blue), due to dose response (green) and due to respiration (red) [9]

High dose gradients in CRT and IMRT make these techniques sensitive to changes of the position and volume of the target in between treatment fractions, which can

last for several weeks. Figure 1.5 shows the temporal changes that can occur in RT, which can be classified into inter-fraction changes, that describe the changes between different treatment fractions and intra-fraction changes that describe the changes within a single treatment fraction. Not taking into account these changes can lead to overdosing OAR or even missing the tumor.

1.1.5.1 Image Guided Radiotherapy (IGRT)

Uncertainties that arise from the patient setup process, can be avoided using image guided radiotherapy (IGRT). In IGRT the tumor and OAR positions are determined immediately before the start of each treatment fraction and are compared with the position at the time of treatment planning. Hence, IGRT requires the use of an imaging system built into the treatment system. In the early years of IGRT portal imaging was used for patient alignment. This technique makes use of the treatment beam and an electronic portal imaging device (EPID). However, this method has a very bad soft tissue contrast. Thus, kilovoltage-imaging devices, such as x-ray tubes or even cone-beam CTs, were incorporated into the treatment systems. The imaging data acquired immediately before treatment using the on-board imaging device, is compared to the planning CT.

1.1.5.2 Adaptive Radiation Therapy (ART)

There may be several weeks between the treatment fractions in RT. During this period, the patient might loose weight, the tumor can change its volume and organs like the bladder or the stomach have different fillings. These changes correspond to anatomical changes and can not simply be accounted for by repositioning the patient, but require an adaption of the treatment plan.

Adaptive Radiation Therapy (ART) customizes the treatment plan to patient-specific variations by monitoring random and systematic errors between CTV and delivered dose distribution during the first few fractions. This is don through image feedback. The PTV is modified based on these variations. A typical interfraction adaptive radiotherapy system consists of 4 steps [10]:

1. *Treatment Delivery*: delivering dose to the patient
2. *Imaging/Verification*: observing and verifying possible variations
3. *Estimation/Evaluation*: estimate the parameters describing the temporal changes and evaluate the corresponding treatment parameters

4. *Adaptive Adjustment*: adapt the treatment plan to fit the temporal new treatment parameters

1.1.5.3 Four Dimensional Radiation Therapy (4DRT)

So far we only discussed inter-fraction motion correction. However, the dose calculation and the treatment plan are only delivered correctly if the tumor remained static during treatment. For tumors of the brain, head, neck and extremities this can be achieved by some kind of immobilization technique. During treatment of thoracic and abdominal tumors, position changes due to respiratory motion have to be considered. For tumors located near the diaphragm the motion amplitude can be as much as three centimeters.

Therefore a lot of research has been put into managing respiratory tumor motion in the last decade. For conventional 3D-CRT this results in larger treatment volumes to encompass the tumor bearing region. This leads to undesired exposure of healthy tissue. However, in recent years tracking based delivery systems were introduced, that track the target and respond to movement in real time so the beam is always following the tumor. This type of treatment is referred to as 4D radiotherapy (4DRT).

1.2 Respiratory Motion Management

Respiratory motion affects all tumors in the thoracic- and abdominal area. Nonetheless, it is of most relevance for lung cancer [11]. The five-year survival rate for lung cancer in Austria is $\sim 24\%$ [12]. In 2005 Machtay et al. showed on >1000 lung cancer patients that higher dose levels result in a decrease in the risk of death [13]. However, lung complications have also been shown to increase with the mean lung dose [14]. Therefore, normal tissue sparing is particularly important for lung tumor patients.

The AAPM Report No. 91 [11] states four measures of respiratory motion management other than the already mentioned encompassing method.

1. *Abdominal compression*: the abdominal motion is restricted to small amplitudes using a pressing plate
2. *Breath-hold methods*: helps to keep the tumor in a certain position for a longer period of time
3. *Respiratory gating*: repeatedly switching the treatment beam off and on depending on whether the tumor is in the treatment field
4. *Real time tumor tracking*: adapting the beam's position to stay fixed to the tumor motion

1.2.1 Abdominal Compression

Forced shallow breathing via abdominal compression was originally introduced by Lax et al. (1994) [15] at the Karolinska Hospital in Stockholm. The method uses a small abdominal pressing plate pressed to the patient's upper abdomen to limit large movements of the diaphragm and thus reduce the tumor movement during respiration.

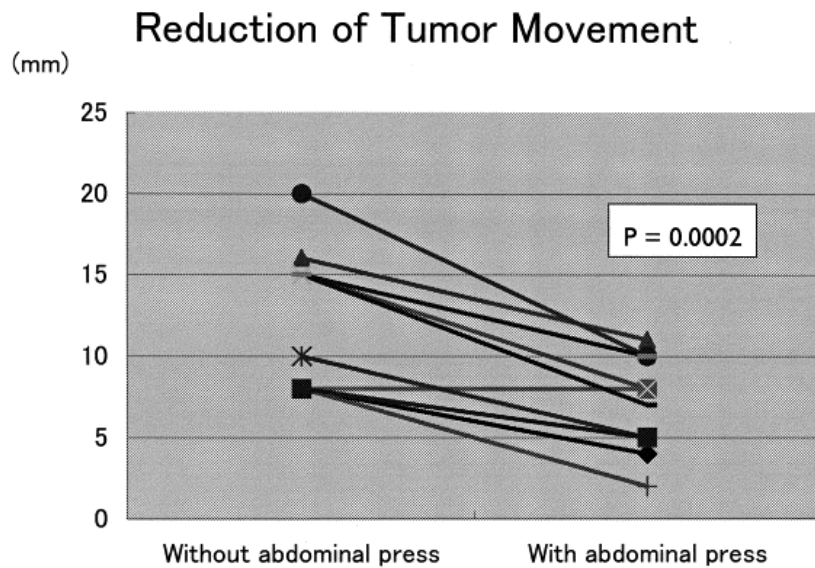


Figure 1.6: Reduction of tumor movement using abdominal compression (image from [16])

Negoro et al. [16] showed on 18 patients with lung tumors that this kind of immobilization technique reduces the tumor movement significantly from a range of 8 to 20 mm to a range of 2 to 11 mm (fig. 1.6).

1.2.2 Breath-Hold Methods

The aim of breath-hold methods is to keep the tumor in a constant position over a larger period of time. Usually breath-hold methods are applied at maximum inhalation or at the end of an exhalation. To achieve reproducibility the patient's breathing is typically monitored using spirometry to measure the patient's lung volume.

The measured data is then either used to actively manipulate the patient's breathing or to coach the patient via audio-visual feedback. Even though both methods are clinically used, patient comfort has to be considered especially for patients with respiratory problems.

1.2.3 Respiratory Gating

Respiratory gating is an intermittent method of dose delivery where radiation is started and stopped at a specific phase in the breathing cycle. The idea of respiratory gating was introduced in 1981 by Jones et al. [17] for the purpose of respiratory

compensation in computed tomography (CT).

In 1989 this method was adopted by Ohara et al. [18] into radiotherapy to solve the problem of tumor movement. Gating strategies often go hand in hand with breath-hold methods to keep the tumor in the desired position for an extended period of time.

An example for a gated treatment system is the Mitsubishi/Hokkaido Real-Time Radio-Therapy (RTRT) system [19], capable of locating gold markers implanted near the tumor via fluoroscopic images. The Mitsubishi/Hokkaido RTRT is discussed in detail in section 1.3.2.1.

1.2.4 Real-Time Tumor Tracking

Although the Mitsubishi/Hokkaido RTRT system is already capable of monitoring the target in real time, the delivery efficiency is reduced as a result of constantly switching off the beam as soon as the tumor moves outside of its intended position. Thus, the last category of managing breathing motion, and undoubtedly the most elegant one, is the so called real-time tumor tracking. In this method, the radiation beam is repositioned dynamically in order to follow the tumor's movement. Real-time tumor tracking can in principle be achieved by a movable linear accelerator, a robotic couch, or a Multileaf Collimator.

The difficulties in implementing a real-time tumor tracking system is to compensate the system's latency times. The latencies of such a system are caused by two things: (1) imaging latency and (2) the response latency of the beam-positioning system.

Imaging latency: If an imaging system is used for target identification, then the time spent acquiring and processing the images contributes to the total latency of the system. This would mean that more lengthy yet often more accurate imaging methods could not be used for tumor monitoring. This problem is dealt with using surrogates that are highly correlated to the tumor motion but easier to monitor. In the case of lung tumors, typically the chest motion is used as a surrogate, which can easily be tracked using pressure belts, infrared tracking or even 3D cameras. The target images are used in parallel to build and maintain the surrogate/tumor correlation. In doing so, the image acquisition and processing can use as much time as needed to get accurate and robust position data.

Another upside of this method is, that the internal imaging frequency can be reduced

without thereby limiting the tracking ability. As a result, the dose delivered to the patient during treatment is drastically reduced.

Response latency: The response of the beam-positioning system usually takes around 100ms [20]. This means that the system has to predict where the target will be when the correction is conducted. For thoracic and abdominal tumors this requires to anticipate the patient's breathing behaviour in advance. This is done by employing prediction algorithms.

The first clinically used system that was capable of real-time tumor tracking was the Cyberknife[®] robotic linear accelerator in combination with the Synchrony[™] Respiratory Tracking System which is described in more detail in section 1.3.2.1.

According to the AAPM report 91 [11] a real-time tumor tracking system has to be able to fulfill four requirements :

1. *identification of the tumor position in real time*
2. *anticipating the tumor motion to allow for time delays in the response of the beam-positioning system*
3. *repositioning the beam*
4. *adapting the dosimetry to allow for changing lung volume and critical structure locations during the breathing cycle*

1. and 2., which outline the main element of this MSc project are further discussed in the following sections.

1.3 Identification of the Tumor

1.3.1 Tumor Localization Methods

Tumor localization methods of thoracic and abdominal tumors can be divided into two main groups, direct and indirect localization. Direct methods localize the tumor by looking directly at it, while indirect methods estimate the tumor position using a surrogate, whose motion is highly correlated to the tumor motion.

Even though direct methods are more precise, indirect methods may present a few advantages, including lower latencies and lower delivery dose.

Clinical applications often take advantage of benefits from both approaches. This results in better accuracy than the indirect methods while bearing less risk to the patient.

1.3.1.1 Direct Methods

Direct methods themselves are in turn classified into non-invasive methods and invasive methods. In invasive methods, markers are implanted in the patient, which can be visualized more easily during the imaging process. Examples for methods that rely on such markers are: electromagnetic transponder based localization, positron emission-based localization and radiographic imaging. The marker position can for instance be calculated by means of simple triangulation. On the other hand, Magnetic Resonance- and Ultrasound based methods function without markers due to their high soft tissue contrast.

There are certain situations where direct marker-less lung tumor tracking via radiographic images is possible. One of the techniques used in such cases, is the so-called **2D/3D registration**.

In 2D/3D registration X-ray image data is compared during the treatment with pre-treatment CT data. If the imaging geometry of an X-ray device is known, for instance by employing a camera-calibration technique, pseudo X-ray images can be generated from the CT, using volume rendering. The acquired image is also called *digitally rendered radiograph* (DRR) [21]. These iteratively produced DRRs are compared to the actual X-ray images until a maximum match is reached. Figure 1.7 shows a reference radiograph compared to a respective DRR. The resulting edge image shows the obtained depth information.

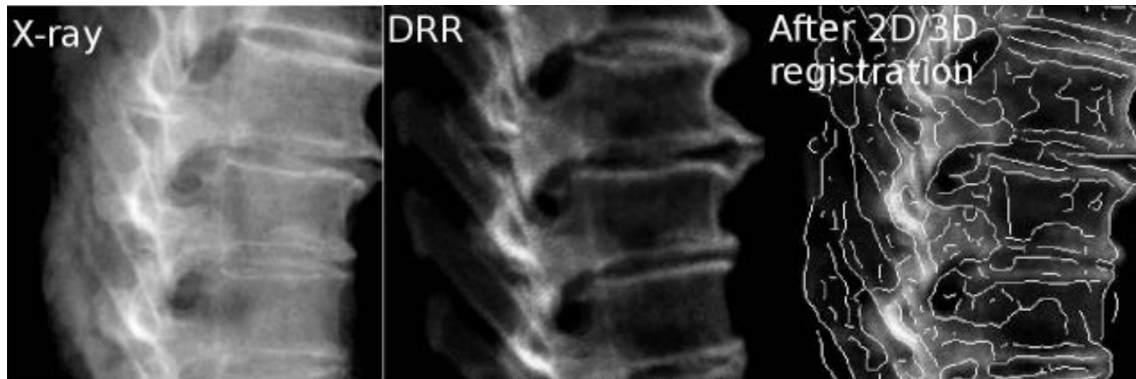


Figure 1.7: Three images showing (from left to right) a reference X-ray, the DRR and the registration result (picture from [21])

1.3.1.2 Indirect Methods

When continuous direct imaging of the tumor is difficult, it could be an advantage to use indirect methods, that infer the tumor position from surrogates. Such surrogates are often easier to monitor. However, they require a strong correlation between the surrogate and the tumor motion. A correlation model has to be build at the beginning of the treatment. Different correlation models will be described in detail in section 1.3.3.

For respiratory tumor motion, there are again two groups of possible surrogates. The first group includes internal surrogates such as the diaphragm motion, while the second group contains external surrogates, such as spectrometry or chest motion. Chest motion is the most commonly used surrogate because of the ease of measuring this movement.

Obviously, surrogate-based methods rely on a preferably stationary correlation over the course of the treatment. This means that a correlation measured at the beginning of the treatment will stay the same over the course of the treatment. However, multiple studies have shown that the correlation is usually not stable and changes with time [22] [23].

Therefore it is necessary to update the correlation during treatment by regularly acquiring additional internal data, that can be paired with the surrogate motion.

1.3.1.3 Hybrid Methods

The third group of localization methods are hybrid methods. Hybrid methods monitor the external respiratory chest motion at a high frequency and simultaneously

acquire internal motion data at a significantly lower frequency. The correlation model parameters are updated accordingly to compensate for the changing correlation.

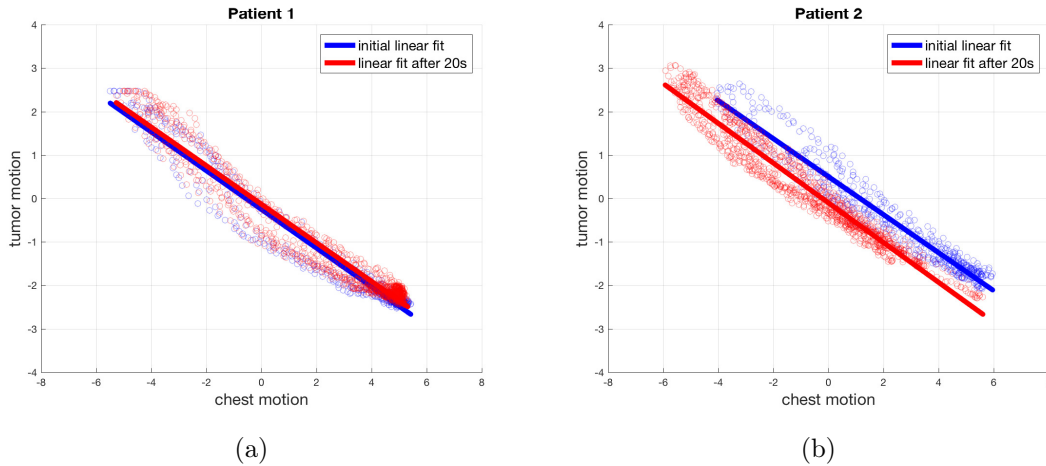


Figure 1.8: Correlation between chest and tumor: a) patient 1 shows a robust correlation b) patient 2 shows a changing correlation

Figure 3.1 illustrates the necessity of correlation updating during therapy for patients with short term correlation. Both fig. 1.8a and fig. 1.8b show the correlation between internal tumor motion and external chest motion taken with a time gap of 20s. It is obvious that patient 1 shows a well-defined correlation over this period of time while the correlation in patient 2 changes considerably.

1.3.2 Localization Tools

As mentioned above, motion-adaptive radiotherapy demands for precise localization of the target in real time. There are different imaging systems to achieve the localization, some of which are already commercially available and clinically used. In this section we discuss the different approaches, and if available, their commercial application.

1.3.2.1 Radiographs

The most commonly used imaging system for tumor tracking are kilovoltage radiographic imaging systems, which can be classified into room mounted and gantry mounted systems. Examples for room mounted systems are the Mitsubishi/Hokkaido

real-time tumor-tracking (RTRT) system, the well known Cyberknife[®] system and the ExacTrac 6D system. Gantry mounted systems include standard C-arm LINACs with built-in kV imaging systems and the MHI vero4DRT system.

The Mitsubishi RTRT system was used to acquire the patient data, which will be used later in this thesis and will therefore be explained hereinafter. Both the MHI vero4DRT and the Cyberknife[®]/Synchrony[™] system employ hybrid methods to achieve dynamic real time tumor tracking and will also be described in detail in the following.



Figure 1.9: Mitsubishi Real Time Tumor Tracking System (picture from [24])

Mitsubishi/Hokkaido RTRT

The Mitsubishi RTRT system was developed in a collaboration between Hokkaido University School of Medicine, Mitsubishi Electronics and the Netherlands Cancer Institute in 2000 [19]. It consists of four sets of X-ray sources and detectors that are mounted to the treatment room. The system is able to monitor the position of a 2mm gold marker which is implanted near the tumor inside the patients body in real time at a 30 Hz sampling rate. The system is used with a stationary linear accelerator and a static couch, i.e. the beam is gated to irradiate as soon as the tumor moves near the isocenter. Fig. 1.9 shows a photograph of the Mitsubishi RTRT. Note that one of the four X-ray tubes is hidden behind the linear accelerator and thus not visible.



(a) Vest with infra-red sensors



(b) infra-red camera



(c) System Setup

Figure 1.10: Cyberknife[®]/Synchrony[™] System (images from [25] and [26])

Cyberknife[®] Synchrony[™]

The Cyberknife[®] system on the other hand only uses two X-ray tubes, that are mounted to the ceiling. The system also comprises a movable linear accelerator (6 degrees of freedom) and a robotic couch. A photograph of the system is shown in figure 1.10.

The robotic couch is used for initial alignment of the patient, in relation to the x-ray tubes using the planning CT. In combination with the Synchrony system, which consists of an infra-red camera and infrared markers that are placed on the patient's chest (fig. 1.10a), the Cyberknife[®] system is capable of performing real time respiratory motion compensation. This is done by using the X-ray imaging

system together with the Synchrony™ system to gather a set of matching tumor and chest data at the beginning of the treatment.

The dataset is then used to build a correlation between chest and tumor motion. During treatment the X-ray imaging system is used for periodically updating the correlation (at intervals of a several seconds to a few minutes).

The Cyberknife® system was the first device that made it possible to move the beam synchronously with the tumor.

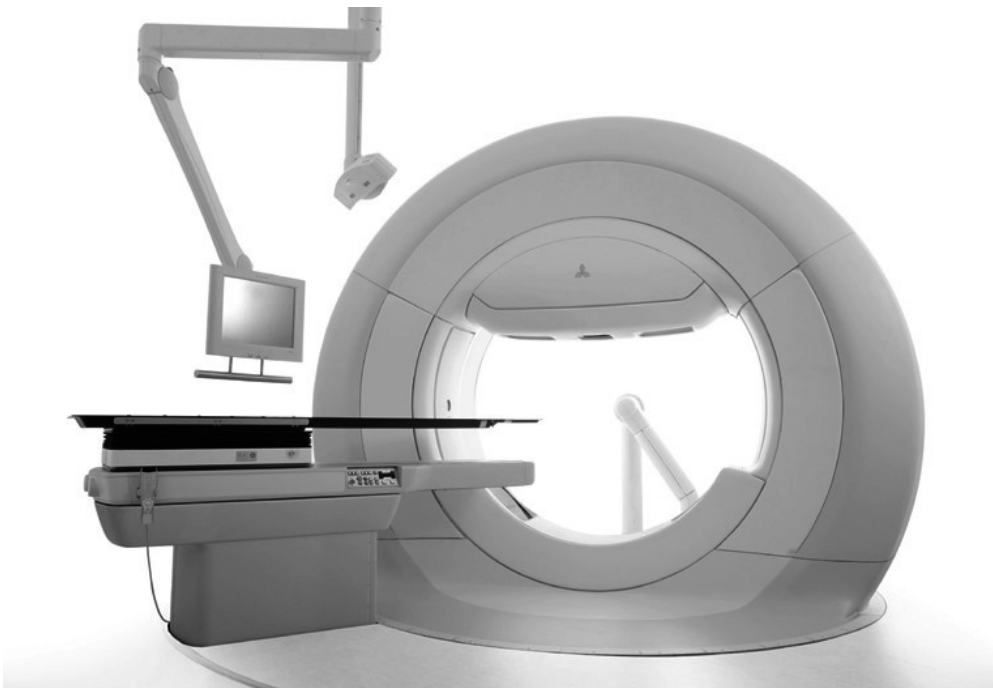


Figure 1.11: MHI 4DRT System (image from [27])

MHI vero4DRT

In 2011, Mitsubishi Heavy Industries launched their dynamic-tracking system, the MHI vero4DRT [27]. The MHI vero4DRT (fig. 1.11) is equipped with two kV-X-ray imaging systems and one MV therapeutic beam that are jointly attached to a gantry. The imaging system and the therapeutic beam can be moved around the patient 360°. Additionally, the gantry can be rotated horizontally. The patient is placed on a robotic couch that is capable of 6-degree-of-freedom movement.

Tracking of the chest motion, similarly to the Synchrony™ system, is done with infrared reflective markers placed on the patients chest and an infrared camera. MHI vero4DRT makes use of gold markers approximately 1.5 mm in diameter, which are inserted near the tumor.

1.3.2.2 Electromagnetic Transponders

In contrast to gold markers that are monitored using ionizing radiation, electromagnetic transponders can be used to track a target inside the body at radio-frequencies [28]. These markers are oscillating circuits that are enclosed in a bio-compatible material. They are excited at different resonance frequencies to induce a response signal. In order to distinguish between multiple markers, all transponders have a different frequency.

A commercially available example for a system using EM-transponders to track prostate tumor motion is the Calypso[®] 4D Localization System[™]. The transponders are 1.8mm in diameter and 8mm in length, and consist of a sealed glass capsule containing an electric circuit [29]. Prior to the treatment ultrasound guidance is used to implant three EM-transponders into the prostate through the rectum. The transponders can be used to track the target at a tracking frequency of 25Hz. The system is able to automatically shut off the beam if the tumor moves out of position. Fig. 1.12a) shows the Calypso[®] 4D Localization System[™].

1.3.2.3 Magnetic Resonance

Magnetic Resonance Imaging (MRI) has the best soft tissue contrast of all discussed imaging methods. Therefore the application in radiotherapy of combining an MR-scanner with a linear accelerator has large potentials. The first design proposition and implementation of a Magnetic Resonance Linac was made by Legendijk et al. in 2008 [30]. It involved a 1.5T Philips Achieva MRI scanner with a Magnex closed bore magnet surrounded by a 6MV Elekta accelerator.

A schematic visualization of such an MR-Linac is shown in figure 1.12b.

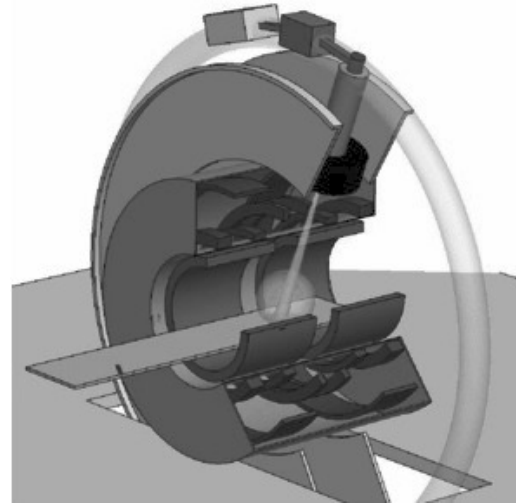
An example for an MR-Linac is the Elekta Unity, presented at the 26th ESTRO in 2017, which will integrate a 1.5 Tesla MR scanner with a linear accelerator. However, the Elekta Unity is not yet available for general sales.

1.3.2.4 Sonography

Another imaging technique for tumor localization is sonography, also known as ultrasound, which was used for a long time in Brachytherapy for seed localization. Ultrasound makes use of pulsed sound waves, that echo off differently on tissues with different densities. Ultrasound imaging is a comparatively cheap method, that can yield 3D data in real time without the use of ionizing radiation.



(a) Calypso[®] 4D Localization System[™]
(image from [31])



(b) MR linac design (picture from [32])

Figure 1.12

In 2005 Hsu et al. [33] performed the first feasibility study using ultrasound for real-time monitoring of tumor motion during radiotherapy. They showed that ultrasound can be used to track soft tissue with sub-millimeter precision.

1.3.3 Correlation Models

Since the application of indirect and hybrid methods present a number of advantages to tumor tracking, in this section we take a closer look at correlation models. These models allow the internal motion to be estimated from external surrogate signals, which are easily acquired with almost no latency. In general, correlation models are build prior to the treatment, but can be updated during treatment. Internal and external data is simultaneously acquired during a *training phase*. A specific correlation model is then fit to the data relating the two signals. During treatment this can be used to estimate the internal tumor position from the external surrogate. In this section we will review the correlation models most commonly used clinically. Additionally we will take a look on how to deal with more complex motion such as **hysteresis**, i.e. the difference in the correlation of chest and lung motion between inhalation and exhalation. Figure 1.13 shows a scatter plot that depicts the motion trajectory of a patient that shows significant hysteresis. For illustrative purposes,

the quadratic inflation and deflation curves are fit to the data

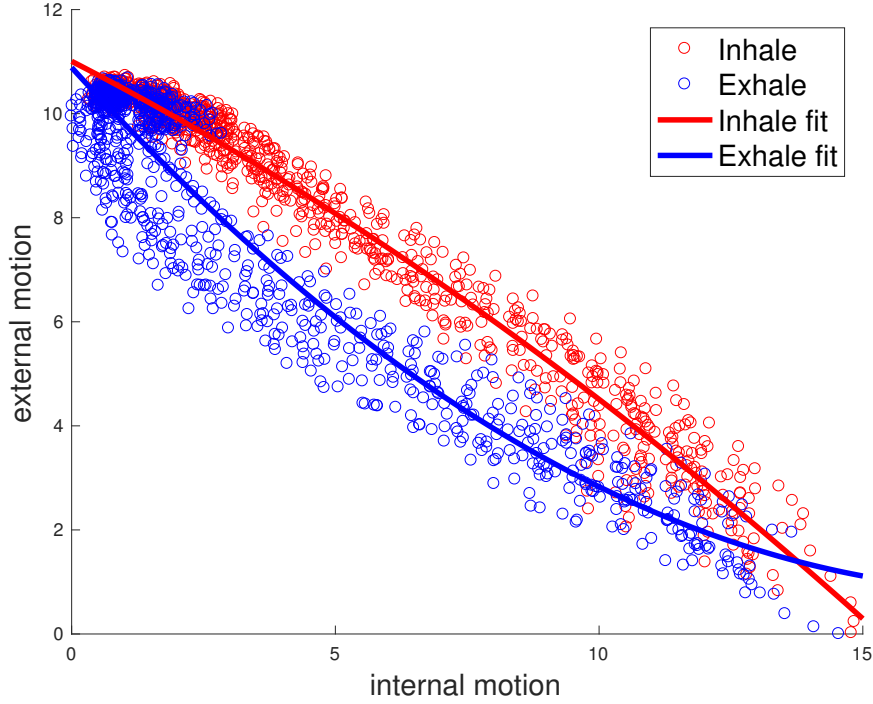


Figure 1.13: Scatter plot of inhalation (red) and exhalation (blue) and their quadratic fit

1.3.3.1 Linear Models

Linear correlation models are by far the most basic and easy to use models. They were first introduced by Schweikard et al. [34] for application in the Cyberknife[®] Synchrony[™] system.

Let's assume we have two training set \mathcal{T}_{int} and \mathcal{T}_{ext} of N corresponding internal- and external data-points. In the case of one dimensional external and internal data, the correlation can be built e.g. using linear regression. The model thus reads,

$$\mathcal{T}_{int} = \alpha + \beta\mathcal{T}_{ext} + \epsilon, \quad \mathbb{E}[\epsilon] = 0, \quad \text{var}[\epsilon] = \sigma^2 \quad (1.1)$$

with the error term ϵ . The estimation of α and β can be made according to the principle of least squares. This is done by minimizing the function,

$$S(\alpha, \beta) = \sum_{i=1}^n (\mathcal{T}_{int,i} - \alpha - \beta\mathcal{T}_{ext,i})^2, \quad (1.2)$$

which leads to

$$\hat{\beta} = \frac{\sum_{i=1}^n \mathcal{T}_{int,i} \mathcal{T}_{ext,i} - n \bar{\mathcal{T}}_{ext} \bar{\mathcal{T}}_{int}}{\sum_{i=1}^n \mathcal{T}_{int,i}^2 - n \bar{\mathcal{T}}_{ext}^2} \quad (1.3)$$

$$\hat{\alpha} = \bar{\mathcal{T}}_{int} - \hat{\beta} \bar{\mathcal{T}}_{ext} \quad (1.4)$$

For the estimation of 3D internal movement a regression model can be fit for every coordinate.

Even though in some cases linear correlation can approximate the respiratory motion well over a short period of time, it can not model hysteresis. This is why 1D correlation has been extended to multivariate linear correlation models. Linear models for multiple surrogate signals were first introduced by Low et al. in 2005 using tidal volume and airflow as surrogates.

Multivariate correlation models do not necessarily need multiple measured surrogates, but often use only one measured surrogate and one derived signal. Using the chest motion and its velocity, the model is able to distinguish between inhalation and exhalation and can thus cope with hysteresis.

Multiple signals that correlate to internal motion corresponds to multivariate regression. In this case the external training matrix \mathcal{T}_{ext} can be represented by a $N \times (m + 1)$ matrix, where N is the number of datapoints and m is the number of signals.

$$\mathcal{T}_{ext} = \begin{pmatrix} 1 & x_{1,1} & \cdots & x_{1,m} \\ 1 & x_{2,1} & \cdots & x_{2,m} \\ \vdots & \vdots & \ddots & \vdots \\ 1 & x_{N,1} & \cdots & x_{N,m} \end{pmatrix} \quad (1.5)$$

The model thus reads,

$$\mathcal{T}_{int} = \mathcal{T}_{ext} \boldsymbol{\beta} + \boldsymbol{\epsilon}, \quad \mathbb{E}[\boldsymbol{\epsilon}] = 0, \quad \text{var}[\boldsymbol{\epsilon}] = \sigma^2 \quad (1.6)$$

The regression coefficient vector is calculated like,

$$\boldsymbol{\beta} = (\mathcal{T}_{ext}^T \mathcal{T}_{ext})^{-1} \mathcal{T}_{ext}^T \mathcal{T}_{int} \quad (1.7)$$

1.3.3.2 Polynomial Models

Another type of correlation models that are widely used are polynomial models. For one dimensional surrogate signals the external training matrix \mathcal{T}_{ext} is represented by

a $N \times (r + 1)$ matrix, where N is the number of datapoints and r is the order of the polynomial function.

$$\mathcal{T}_{ext} = \begin{pmatrix} 1 & x_1 & x_1^2 & \cdots & x_1^r \\ 1 & x_2 & x_2^2 & \cdots & x_2^r \\ \vdots & \vdots & \vdots & \ddots & \vdots \\ 1 & x_N & x_N^2 & \cdots & x_N^r \end{pmatrix} \quad (1.8)$$

The regression coefficients are calculated analogous to equation 1.7.

Polynomial models are able to describe more complicated correlation paths. However, they are not suited for extrapolation. This means that if data during treatment lies outside the training data, large extrapolation errors may occur. Therefore, it makes sense to fall back to a linear model for surrogate signals that lie outside the range of the training data.

The generalization of polynomial models to multivariate input data is straightforward and analogous to generalization of linear models. The external training matrix \mathcal{T}_{ext} is now represented by a $N \times (1 + m \cdot r)$ matrix.

$$\mathcal{T}_{ext} = \begin{pmatrix} 1 & x_{1,1} & \cdots & x_{1,m} & x_{1,1}^2 & \cdots & x_{1,m}^2 & x_{1,1}^r & \cdots & x_{1,m}^r \\ 1 & x_{2,1} & \cdots & x_{2,m} & x_{2,1}^2 & \cdots & x_{2,m}^2 & x_{2,1}^r & \cdots & x_{2,m}^r \\ \vdots & \vdots & \ddots & \vdots & \vdots & \ddots & \vdots & \vdots & \ddots & \vdots \\ 1 & x_{N,1} & \cdots & x_{N,m} & x_{N,1}^2 & \cdots & x_{N,m}^2 & x_{N,1}^r & \cdots & x_{N,m}^r \end{pmatrix} \quad (1.9)$$

A polynomial model with a one dimensional surrogate signal is not able to model hysteresis as the correlation must be the same during inhalation and exhalation. This restriction can be avoided by fitting two separate polynomials, one to the data from inhalation and one to the data from exhalation, as illustrated in fig. 1.13. However, this may result in discontinuities of the motion estimates when switching from inhale to exhale.

1.3.3.3 Principal Component Analysis

Multidimensional surrogate data is often highly correlated. Therefore it makes sense to reduce the dimensionality of such data. In practice, this is done using Principal Component Analysis (PCA). Let's assume that the multidimensional data is represented by a d -dimensional random vector $\mathbf{X} = (X_1, \dots, X_d)^T$ that follows a

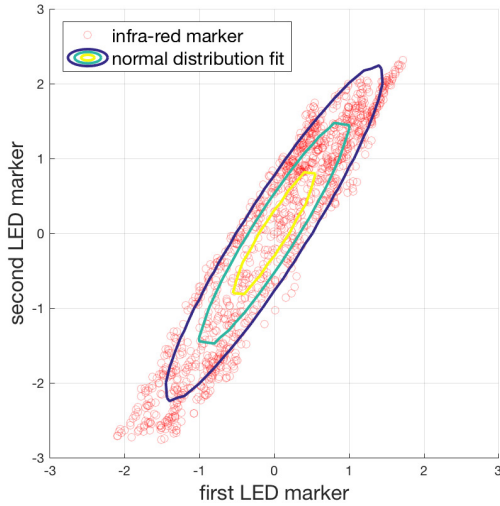
joint probability distribution. The matrix \mathbf{C} , defined as

$$C_{i,j} = \text{cov}[X_i, X_j] \quad (1.10)$$

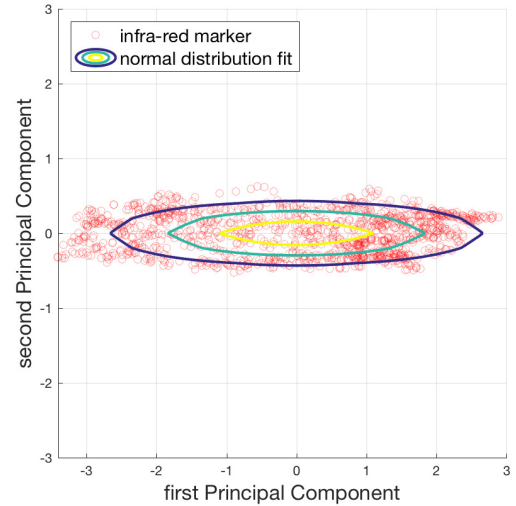
is the $d \times d$ covariance matrix of \mathbf{X} . It contains the variances in the diagonal and the pairwise covariances in the off-diagonal of all components of \mathbf{X} . The covariance matrix is a symmetric, positive definite matrix, and can therefore be diagonalized. In fact, the Principle Component Analysis is nothing more than the diagonalization of the covariance matrix, $\mathbf{D} = \mathbf{U}\mathbf{C}\mathbf{U}^T$, where \mathbf{U} is the orthogonal transformation matrix. The column vectors of \mathbf{U} are the eigenvectors of \mathbf{C} .

As an example for a 2D PCA, figure 1.14a shows the scattered data for two infrared markers. The multivariate data was provided courtesy of Robert Dürichen [35]. For illustration purposes the contours of the fitted bivariate normal distribution are also shown. In two dimensions the rotation matrix \mathbf{U} simplifies to

$$\mathbf{U} = \begin{pmatrix} \cos\phi & -\sin\phi \\ \sin\phi & \cos\phi \end{pmatrix} \quad \text{with } \phi = -\frac{1}{2} \text{arccot} \left(\frac{C_{1,1} - C_{2,2}}{2C_{1,2}\sqrt{C_{1,1}C_{2,2}}} \right). \quad (1.11)$$



(a) IR-marker position in the original coordinate system (the first and the second LED marker position are highly correlated)



(b) IR-marker position in principal component coordinate system (no correlation between 1st and 2nd principal component)

Figure 1.14: Scatter data of the infrared markers with a bivariate normal distribution fit for illustration purposes

Figure 1.14b shows the rotated, uncorrelated scattered data in principle component space.

1.3.3.4 Other Models

Other more complex correlation models have been suggested in the literature including neural networks, support vector regression and fuzzy logic [36]. These models are often extremely computationally expensive and are therefore unsuitable for clinical application. For further information on these models readers should refer to the literature mentioned above [36].

1.4 Anticipating the Tumor Motion

To account for small latencies of the beam positioning system, the tumor motion has to be anticipated. Over the last few years a variety of different methods to the problem of respiratory motion prediction have been introduced . Basically, these methods can be categorized into two different approaches: (1) *model-based approaches*, that make a priori assumptions about an underlying motion model and (2) *model-free approaches*, where no biomechanical assumptions about the breathing motion have to be made beforehand.

Examples for model-based methods are the *Sinoidal Model* and *Kalman Filtering*. Model-free prediction include for example *Adaptive Filtering* or *Artificial Neural Networks*. In the following sections, a small selection of these methods are briefly discussed.

1.4.1 Model-based Prediction

1.4.1.1 Sinoidal Model

The motivation for a Sinoidal Model stems from the semi-periodic sinusoidal nature of respiratory motion and was first described by Vedam et al. [37]. A sinus curve can be fitted to respiratory motion over a signal history length N . Let $\mathbf{y}(t) = (y_t, y_{t-1}, \dots, y_{t-N})^T$ be the signal history vector at time t and $f(\beta_i, t) = \beta_1 \sin(\beta_2 t + \beta_3) + \beta_4$ be the sinusoidal fitting function. To find the values for β_i the minimization problem,

$$\min_{\beta_i} [S(\beta_i)] \quad \text{with} \quad S(\beta_i) = \sum_{j=0}^{j=N} r_j(\beta_i)^2 = [y_{t-j} - f(\beta_i, t - j)]^2 \quad (1.12)$$

has to be solved. This can be done e.g. using the Gauss-Newton algorithm, by iteratively improving an initial guess of β_i :

$$\beta_i = \beta_i + \alpha \cdot (J^T J)^{-1} J^T r_i \quad (1.13)$$

where J is the Jacobian of f and α is a damping factor.

At each time instant t_i a new minimization problem is solved to find the current

best fit for β_i . The predicted position is now given by,

$$y_{pred}(t + \delta) = y_t + [f(\beta_i, t + \delta) - f(\beta, t)]. \quad (1.14)$$

1.4.1.2 Kalman Filter

The Kalman filter is a Bayesian method that can be used to predict future states of a linear state-space model. The states are discretized in the time domain and are represented by the set of variables describing the dynamics of the system. At each point in time a linear operator, the state transition operator \mathbf{F}_{k-1} , is applied to the state $\hat{\mathbf{x}}_{k-1}$ to generate a new state $\hat{\mathbf{x}}_k$. The state transition operator captures the dynamics of the system, therefore represents the underlying motion model. Additionally, the new state vector $\hat{\mathbf{x}}_k$ is influenced by deterministic external forces represented by the control vector $\hat{\mathbf{u}}_{k-1}$ and the control matrix \mathbf{B}_{k-1} . The uncertainty of the state transition follows a normal distribution with zero mean and covariance matrix \mathbf{Q}_k , hence is given by $\mathbf{w}_k \sim \mathcal{N}(0, \mathbf{Q}_k)$. Thus the states evolve like:

$$\hat{\mathbf{x}}_k = \mathbf{F}_{k-1}\hat{\mathbf{x}}_{k-1} + \mathbf{B}_{k-1}\hat{\mathbf{u}}_{k-1} + \mathbf{w}_k. \quad (1.15)$$

In order to use the measurements of the system, they have to be mapped to state space. This is done with the observation model \mathbf{H}_k . The measurement \mathbf{v}_k noise is assumed to be uncorrelated and normally distributed $\mathbf{v}_k \sim \mathcal{N}(0, \mathbf{R}_k)$. The observation equation thus reads,

$$\hat{\mathbf{z}}_k = \mathbf{H}_k\hat{\mathbf{x}}_k + \mathbf{v}_k. \quad (1.16)$$

Kalman filtering is based on two steps: (1) Prediction, where the model is used to calculate the new state and (2) Updating, which uses the measurement to refine the state estimate.

1. Prediction: The state dynamics are used to calculate the a-priori state prediction and the a-priori prediction of the covariance matrix of the state vector \mathbf{P}_k .

$$\hat{\mathbf{x}}_{k|k-1} = \mathbf{F}_k\hat{\mathbf{x}}_{k-1|k-1} + \mathbf{B}_k\hat{\mathbf{u}}_k \quad (1.17)$$

$$\hat{\mathbf{P}}_{k|k-1} = \mathbf{F}_k\hat{\mathbf{P}}_{k-1|k-1}\mathbf{F}_k^T + \mathbf{Q}_k \quad (1.18)$$

2. Update: The prediction is then refined using the measurement.

$$\hat{\mathbf{x}}_{k|k} = \hat{\mathbf{x}}_{k|k-1} + \hat{\mathbf{K}}_k \tilde{\mathbf{y}}_k \quad (1.19)$$

$$\hat{\mathbf{P}}_{k|k} = \hat{\mathbf{P}}_{k|k-1} - \hat{\mathbf{K}}_k \mathbf{S}_k \hat{\mathbf{K}}_k^T \quad (1.20)$$

with the residual $\tilde{\mathbf{y}}_k$, the residual covariance \mathbf{S}_k and the Kalman gain $\hat{\mathbf{K}}_k$.

$$\tilde{\mathbf{y}}_k = \mathbf{z}_k - \mathbf{H}_k \hat{\mathbf{x}}_{k|k-1} \quad (1.21)$$

$$\mathbf{S}_k = \mathbf{H}_k \hat{\mathbf{P}}_{k|k-1} \mathbf{H}_k^T + \mathbf{R}_k \quad (1.22)$$

$$\hat{\mathbf{K}}_k = \hat{\mathbf{P}}_{k|k-1} \mathbf{H}_k^T \mathbf{S}_k^{-1} \quad (1.23)$$

The generalization of the Kalman Filter to non-linear state transition operators \mathbf{F}_k is called the *Extended Kalman Filter (EKF)*. The EKF allows modeling with arbitrary functions $f(\hat{\mathbf{x}}_k)$ by replacing \mathbf{F}_k with its Jacobi Matrix.

$$\mathbf{F}_k = \left. \frac{\partial f}{\partial \mathbf{x}} \right|_{\hat{\mathbf{x}}_{k-1|k-1}} \quad (1.24)$$

For the application of EKF for respiratory motion prediction, different motion models have been suggested. Ramrath et al. [38] for example proposed a model that is based on the assumption that multiple sinusoidal components contribute to respiratory motion. Hong et al. [39] suggested to model the motion of the signal with respect to a delayed signal, which leads to a locally circular motion. This model is further discussed in section 2.3.

The great advantage of Kalman Filters is the low computational cost.

1.4.2 Model-free Prediction

1.4.2.1 Adaptive Filtering

An adaptive filter is a time-variant system that automatically adapts its parameters with a recursive algorithm. This process is called self alignment.

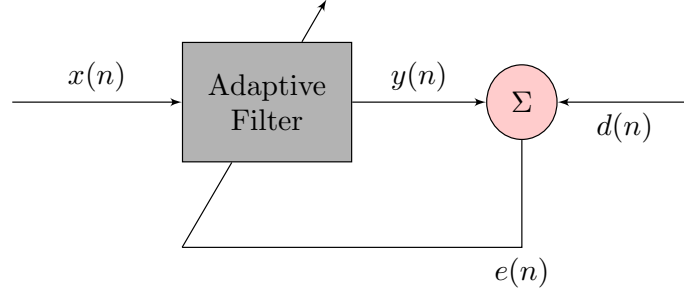


Figure 1.15: Adaptive filtering flowchart

Figure 1.15 shows the working flow of an adaptive filter. At every time-step n the output response $y(n)$ is calculated from the input signal $x(n)$. The error $e(n)$ is calculated from the desired response $d(n)$. The error signal is fed back into the filter which adapts its parameters from time n to time $n + 1$. With increasing time, the output response $y(n)$ should converge towards $d(n)$.

The typical filter structure is given by,

$$y(n) = \sum_{i=0}^M w_i(n)x(n-i), \quad (1.25)$$

with $w_i(n)$ being the filter weights and M being the number of filter taps, i.e. the signal history that is used for prediction. After every time step the the weights are updated as follows:

$$w(n+1) = w(n) + \mu f(e(n), x(n)), \quad (1.26)$$

where μ is the step size and $f(e(n), x(n))$ is a vector valued function. Adaptive filtering is widely used in the literature to predict respiratory motion [37, 40, 41]. The biggest problem of adaptive algorithms is the difficulty of selecting the right learning parameter μ and the signal history length M . Slightly off starting values can cause the algorithm to converge [41].

1.4.2.2 Neural Networks

The concept of artificial neural networks (ANN) is based on the neural structure of the brain. A typical ANN consists of an input layer, (multiple) hidden layers and an output layer. Each layer consist of multiple nodes, that are connected to every node of the previous and next layer with weights. The layers calculate their output with a predefined so called activation function, which is a function of the previous layer result and the weights. Figure 1.16 shows an ANN with a single hidden layer

with input x_i , hidden layer output y_j and output z_k . The weights are denoted w_{ji} and v_{kj} and the activation functions are given by $f(w_{ji}, x_i)$ and $g(v_{kj}, y_j)$.

In order to use the neural network as a prediction tool, it needs to learn the behaviour of the system from prior input and output data. This so called supervised learning is performed in three phases.

1. Learning phase: the ANN is presented with paired input and output data in order to train the model (change the weights to fit the data).
2. Validation phase: to be able to estimate how well ANN works on data that was not part of the learning data. The results of the validation phase represent the quality of the predictor.
3. Application phase: the ANN is now applied to real world data to predict future values.

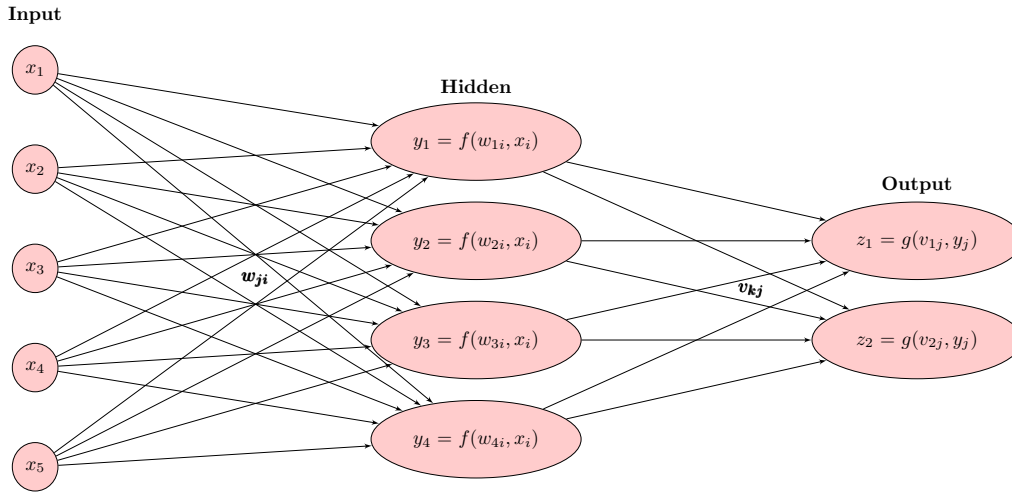


Figure 1.16: Artificial neural network with three layers and interconnected nodes

Sharp et al. [42] introduced an ANN predictor for respiratory motion. They use an ANN with one hidden layer with a sigmoid non-linear activation function. The hidden layer output y_j is calculated as

$$y_j = \frac{1}{1 + \exp(-\sum w_{ij}x_i)}, \quad (1.27)$$

with the weights w_{ij} and the input x_i . The output layer uses a linear activation function, hence the output z_i is given by

$$z_k = \sum w_{jk}y_j. \quad (1.28)$$

Artificial neural networks are extremely computationally expensive, which makes on-line updating difficult.

1.5 Motivation

The aim of this work was to build an algorithm in C++, that is capable of compensating the latency of a system where the tumor monitoring is difficult and shows an extremely high latencies. In particular we focus on lung tumors, that are monitored using 2D/3D registration. This is achieved by using the previously mentioned correlation approach. Two different previously published correlation models used in the MHI vero4DRT and the Cyberknife[®]/ Synchrony[™] system were implemented. The correlation parameters can be iteratively updated during treatment by acquiring new internal data. Additionally a prediction algorithm was implemented to correct for small latencies of the beam-positioning system. This is done by employing an Extended Kalman Filter with a Local Circular Motion model of the respiratory motion. Multiple safety mechanisms are included to avoid undesired radiation during irregular and unpredictable motion. The provided algorithm is not limited to specific sampling frequencies or latencies and can be used in a vast variety of cases.

Chapter 2

Methods

In this section we will describe the different methods, that were evaluated in this MSc project and implemented in the provided C++ algorithm. The algorithm should be able to work with an arbitrary yet small internal imaging frequency with a very high latency and additionally compensate smaller latencies of the control system. The aim of the algorithm is to provide stable results, suitable for clinical use. Therefore we use the two most widely, clinically used correlation methods, namely the Cyberknife[®] Synchrony[™] and the MHI vero4DRT method. An Extended Kalman filter with the Local Circular Motion Model (LCM) was used for ahead prediction.

2.1 Cyberknife[®] Synchrony[™] Correlation Method

Ernst et al. provided a detailed description of the Cyberknife model [43]. The model uses two 2^{nd} order polynomial functions, one for inhalation and one for exhalation. This way it can deal with the problem of hysteresis as discussed in section 1.3.3.2. Additionally, a smoothing mechanism is build into the model, which blends the two polynomials near the end of inhalation and exhalation to prevent abrupt transition between them. Furthermore, a linear fall back mechanism is applied to prevent large errors for external data-points located outside of the training data.

Let's assume we have a training set \mathcal{T} consisting of N samples of corresponding internal and external data. This means that every data-point in this set contains both the position of the tumor and the surrogate. Assuming 3D internal data (x, y, z) and 1D external data e , one point can be represented by a vector $p_i = (x_i, y_i, z_i, e_i)^T$. In order to build different correlation functions for inhalation and exhalation the

training set \mathcal{T} has to be divided into subsets for inhalation \mathcal{T}_{in} and exhalation \mathcal{T}_{ex} . This is done by using the velocity of the external data $v_{e_i} = \frac{e_i - e_{i-1}}{\Delta t}$, and using a threshold velocity v_{th} :

$$v_{e_i} \geq v_{th} \rightarrow \mathcal{T}_{in} \quad (2.1)$$

$$v_{e_i} \leq -v_{th} \rightarrow \mathcal{T}_{ex} \quad (2.2)$$

$$v_{th} > v_{e_i} > -v_{th} \rightarrow \mathcal{T}_{in} \ \& \ \mathcal{T}_{ex} \quad (2.3)$$

This way, samples with low speed at the end of inhale end exhale are sorted into both \mathcal{T}_{in} and \mathcal{T}_{ex} . These sets are used to build two quadratic correlation functions.

The respiratory movement and the breathing amplitudes can change over the course of the treatment. This can lead to data points that lie outside the extremes of the training set. Since the quadratic function is not suitable for extrapolation, this could lead to large errors. For this reason, a *linear fallback mechanism* is included in the model. Additionally to the two quadratic correlation functions, a third, linear function is calculated which is used as soon as the observed external datapoint lies outside the training set.

Lastly, the blending mechanism ensures the smooth transition between all three functions. Note that the blending mechanism described in [43] has some flaws.

Let

$$r_1 = \min(\mathcal{T}_{ext}) \quad (2.4)$$

$$r_2 = \max(\mathcal{T}_{ext}) \quad (2.5)$$

$$r_3 = \sigma (r_2 - r_1), \quad (2.6)$$

where \mathcal{T}_{ext} is the external part of the training set \mathcal{T} (not to be confused with the exhalation subset \mathcal{T}_{ex}) and σ is the overlap parameter (percentage of overlap). Now,

six subsets with specific limits are defined:

$$\mathcal{R}^- = [r_1 + 2r_3, r_2 - 2r_3] \quad (2.7)$$

$$\mathcal{R}_1^{\leftarrow} = [r_1 + r_3, r_1 + 2r_3] \quad (2.8)$$

$$\mathcal{R}_1^{\rightarrow} = [r_2 - 2r_3, r_2 - r_3] \quad (2.9)$$

$$\mathcal{R}_2^{\leftarrow} = [r_1 - r_3, r_1 + r_3] \quad (2.10)$$

$$\mathcal{R}_2^{\rightarrow} = [r_2 - r_3, r_2 + r_3] \quad (2.11)$$

$$\mathcal{R}^+ = \mathcal{R}^- \cup \mathcal{R}_1^{\leftarrow} \cup \mathcal{R}_1^{\rightarrow} \cup \mathcal{R}_2^{\leftarrow} \cup \mathcal{R}_2^{\rightarrow}. \quad (2.12)$$

The meaning of these sets is illustrated in figure 2.1.

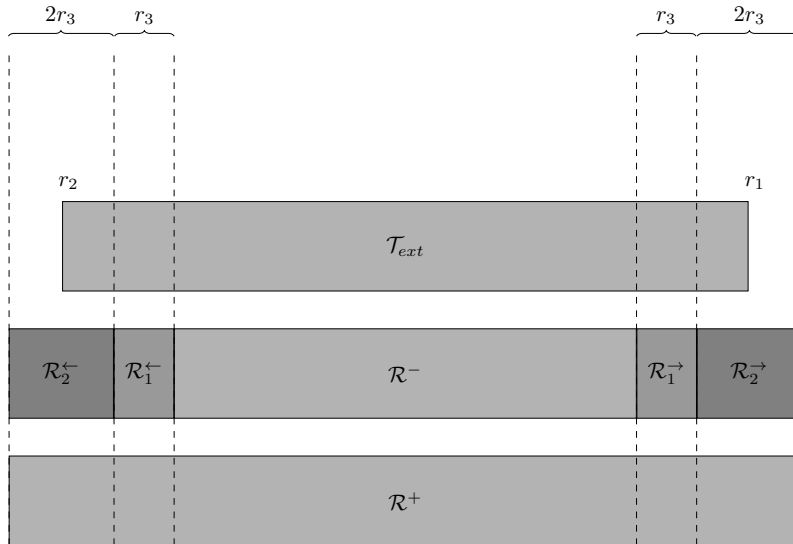


Figure 2.1: Illustration of blending sets and limits

With

$$d_1^{\leftarrow}(e) = \frac{e - r_1 - 2r_3}{-r_3} \quad (2.13)$$

$$d_1^{\rightarrow}(e) = \frac{e - r_2 + 2r_3}{r_3} \quad (2.14)$$

$$d_2^{\leftarrow}(e) = \frac{e - r_1 - r_3}{-2r_3} \quad (2.15)$$

$$d_2^{\rightarrow}(e) = \frac{e - r_2 + r_3}{2r_3}, \quad (2.16)$$

where x_i is a new external data point and v_i is its velocity, the blended correlation

function reads:

$$f(e) = \begin{cases} f_{\text{in}}(e) & \text{if } e \in \mathcal{R}_1^{\rightarrow} \cap v_e > 0 \\ f_{\text{ex}}(e) & \text{if } e \in \mathcal{R}_1^{\rightarrow} \cap v_e < 0 \\ [1 - d_1^{\rightarrow}(e)] f_{\text{in}}(e) + d_1^{\rightarrow}(e) \frac{1}{2} [f_{\text{in}}(e) + f_{\text{ex}}(e)] & \text{if } e \in \mathcal{R}_1^{\rightarrow} \cap v_e > 0 \\ [1 - d_1^{\rightarrow}(e)] f_{\text{ex}}(e) + d_1^{\rightarrow}(e) \frac{1}{2} [f_{\text{in}}(e) + f_{\text{ex}}(e)] & \text{if } e \in \mathcal{R}_1^{\rightarrow} \cap v_e < 0 \\ [1 - d_1^{\leftarrow}(e)] f_{\text{in}}(e) + d_1^{\leftarrow}(e) \frac{1}{2} [f_{\text{in}}(e) + f_{\text{ex}}(e)] & \text{if } e \in \mathcal{R}_1^{\leftarrow} \cap v_e > 0 \\ [1 - d_1^{\leftarrow}(e)] f_{\text{ex}}(e) + d_1^{\leftarrow}(e) \frac{1}{2} [f_{\text{in}}(e) + f_{\text{ex}}(e)] & \text{if } e \in \mathcal{R}_1^{\leftarrow} \cap v_e < 0 \\ [1 - d_2^{\leftarrow}(e)] \frac{1}{2} [f_{\text{in}}(e) + f_{\text{ex}}(e)] + d_2^{\leftarrow}(e) f_{\text{lin}}(e) & \text{if } e \in \mathcal{R}_2^{\leftarrow} \\ [1 - d_2^{\rightarrow}(e)] \frac{1}{2} [f_{\text{in}}(e) + f_{\text{ex}}(e)] + d_2^{\rightarrow}(e) f_{\text{lin}}(e) & \text{if } e \in \mathcal{R}_2^{\rightarrow} \\ f_{\text{lin}}(e) & \text{if } e \notin \mathcal{R}^+. \end{cases}$$

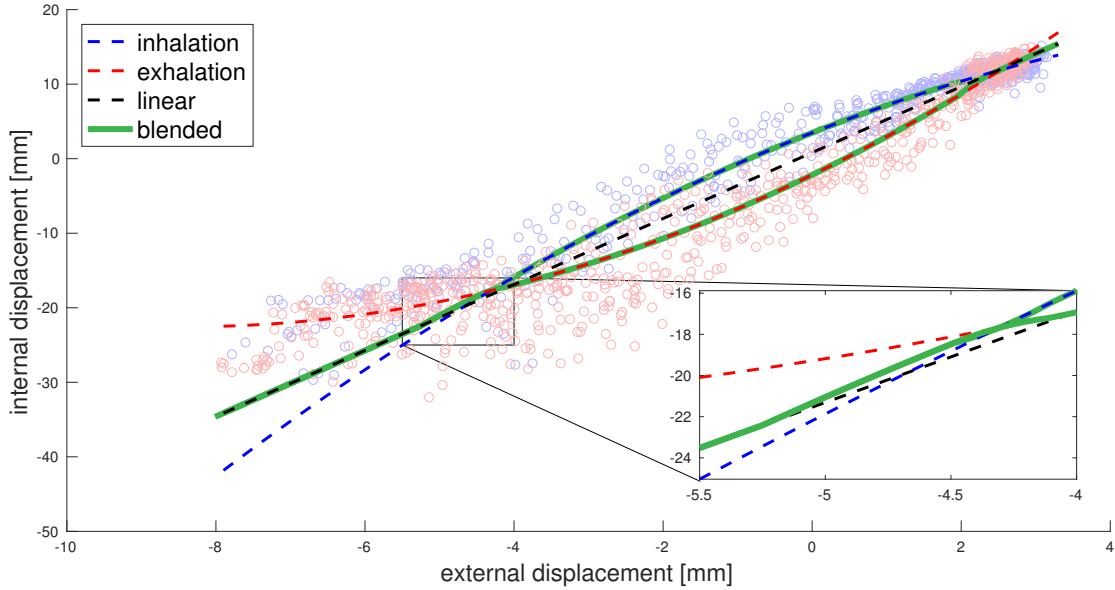


Figure 2.2: Illustration on how the blending mechanism works: scatter plot of breathing data and their correlation functions and close up of the transition between the correlation functions; for illustration purposes one patient showing large hysteresis was chosen; the patient data was acquired at the Mitsubishi RTRT system [44]

Figure 2.2 illustrates how the blending mechanism works. It shows the quadratic correlations of inhale and exhale, the linear fallback correlation and the blended correlation function.

2.2 MHI vero4DRT Corrleation Method

The MHI vero4DRT correlation model takes a different approach to deal with hysteresis. It makes use of a 2^{nd} order polynomial multivariate correlation function, dependent on both the position e and the velocity v_e of the external chest motion. Thus, there is no need for two separate correlation functions for the breathing phases (inhalation & exhalation). The change in sign in the velocity between inhalation ($v_e > 0$) and exhalation ($v_e < 0$) automatically takes care of hysteresis. The model is given by,

$$f(e) = \beta_0 + \beta_1 \cdot e + \beta_2 \cdot e^2 + \beta_3 \cdot v_e + \beta_4 \cdot v_e^2. \quad (2.17)$$

Note that Poels et al. showed in 2015 that both correlation methods are interchangeable in terms of geometrical accuracy when modelled with an 11Hz full fluoroscopy sequence [45].

2.3 Local Circular Motion Model

For prediction we used an Extended Kalman Filter with the Local Circular Motion (LCM) Model, suggested by Hong et al. in 2010 [39] to describe the local dynamics of breathing motion.

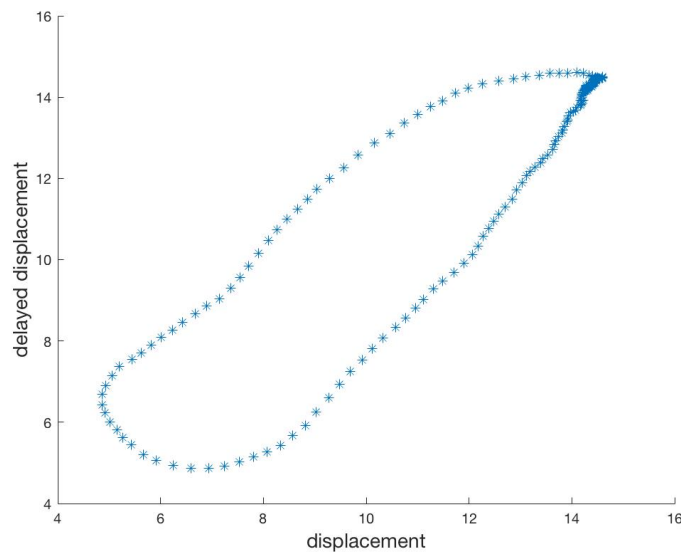


Figure 2.3: Breathing trajectory in augmented space

The idea is to create a new coordinate system with the x-axis being the current tumor displacement and the y-axis being the past displacement. This new coordinate system is referred to as the augmented coordinate plane. In this augmented space the breathing trajectory is a *time-varying quasi-ellipse*. Figure 3.3 shows such a quasi ellipse for a temporal delay of 0.3 seconds. With this approach, we can model the trajectory locally as circular motion, hence the name Local Circular Motion Model. More precisely, the ellipse is treated locally like the arc of a circle, and the motion along the ellipse is treated like circular motion.

The differential equations of circular motion read,

$$\ddot{x}(t) = -\omega \cdot \dot{y}(t) \quad (2.18)$$

$$\ddot{y}(t) = -\omega \cdot \dot{x}(t) \quad (2.19)$$

$$\dot{\omega} = 0. \quad (2.20)$$

Using the state vector $\mathbf{x}(t) = (x(t), \dot{x}(t), \dot{y}(t), \omega)^T$ the differential equations can be rewritten as,

$$\dot{\mathbf{x}}(t) = \mathbf{A}\mathbf{x}(t). \quad (2.21)$$

with

$$\mathbf{A} = \begin{pmatrix} 0 & 1 & 0 & 0 \\ 0 & 0 & -\omega & 0 \\ 0 & \omega & 0 & 0 \\ 0 & 0 & 0 & 0 \end{pmatrix}. \quad (2.22)$$

Discretization of this equation leads to,

$$\mathbf{x}(k+1) = \mathbf{A}_d \mathbf{x}(k). \quad (2.23)$$

with

$$\mathbf{A}_d = \exp(\mathbf{A}t), \quad (2.24)$$

where k denotes the current time index and t is the time between two steps.

The matrix \mathbf{A} is diagonalizable and therefore \mathbf{A}_d can be calculated as follows:

$$\mathbf{A}_d = \mathbf{T} \exp(\mathbf{D}t) \mathbf{T}^{-1}, \quad (2.25)$$

with \mathbf{D} being the diagonal form of \mathbf{A} :

$$\mathbf{A} = \mathbf{T}\mathbf{D}\mathbf{T}^{-1}. \quad (2.26)$$

Here one can exploit that the exponential of a diagonal matrix can be determined by applying the exponential function to each diagonal entry. This leads to the discretized matrix,

$$\mathbf{A}_d = \begin{pmatrix} 1 & \frac{\sin(\omega_k t)}{\omega_k} & -\frac{1-\cos(\omega_k t)}{\omega_k} & 0 \\ 0 & \cos(\omega_k t) & -\sin(\omega_k t) & 0 \\ 0 & \sin(\omega_k t) & \cos(\omega_k t) & 0 \\ 0 & 0 & 0 & 1 \end{pmatrix}. \quad (2.27)$$

The time evolution of the components can therefore be written as,

$$x_{k+1} = x_k + \frac{\sin(\omega_k t)}{\omega_k} \dot{x}_k - \frac{1 - \cos(\omega_k t)}{\omega_k} \dot{y}_k \quad (2.28)$$

$$\dot{x}_{k+1} = \cos(\omega_k t) \dot{x}_k - \sin(\omega_k t) \dot{y}_k \quad (2.29)$$

$$\dot{y}_{k+1} = \sin(\omega_k t) \dot{x}_k + \cos(\omega_k t) \dot{y}_k \quad (2.30)$$

$$\omega_{k+1} = \omega_k \quad (2.31)$$

The true position $x(k)$ is measured with a noise w_k leading to the measurement of z_k .

$$z_k = x_k + w_k \quad (2.32)$$

Assuming, that we have made N measurements $z(i)$ so far. These measurements are combined in the set $Z^k = [z(1), \dots, z(N)]^T$.

Using the model introduced above, future observations can be predicted using,

$$\mathbf{x}_{k+1} = \mathbf{A}_d(\mathbf{x}_k)\mathbf{x}_k = f(\mathbf{x}_k). \quad (2.33)$$

Note that the state equation 2.33 is a non-linear equation in ω . This is because the transition matrix \mathbf{A}_d itself depends on the state \mathbf{x}_k .

In order to account for deviations of the model, we introduce a zero mean, white

noise vector $\mathbf{v}(k)$ that describes the inaccuracy of this model. The model thus reads,

$$\mathbf{x}_{k+1} = f(\mathbf{x}_k)\mathbf{x}_k + \mathbf{v}_k. \quad (2.34)$$

The covariance matrix of the noise vector is assumed to look like,

$$\mathbf{Q}_k = \begin{pmatrix} \frac{1}{3}q_1T^3 & \frac{1}{2}q_1T^2 & 0 & 0 \\ \frac{1}{2}q_1T^2 & q_1T & 0 & 0 \\ 0 & 0 & q_2T & 0 \\ 0 & 0 & 0 & q_3T \end{pmatrix}, \quad (2.35)$$

meaning that x and \dot{x} are correlated, while \dot{x} , \dot{y} and $\dot{\omega}$ are mutually uncorrelated. The parameters q_i are free parameters of the system and have to be set manually. With the introduction of this covariance matrix, specifically q_3 , the angular velocity ω can now change over time depending on the Kalman gain. This means, that depending on how good the prediction is compared to the measurement the angular velocity ω gradually changes to find the optimum value.

The measurement noise $w(k)$ is also assumed to be white noise with zero mean. In terms of the observation matrix $\mathbf{H} = (1, 0, 0, 0)^T$ the observation model reads,

$$z_k = \mathbf{H}\mathbf{x}_k + w_k \quad (2.36)$$

The above mentioned non-linearity of the state equation 2.33 requires non-linear state prediction, hence Extended Kalman Filtering.

Therefore the one step prediction reads,

$$\hat{\mathbf{x}}_{k+1|k} = f(\hat{\mathbf{x}}_{k|k}) \quad (2.37)$$

$$\mathbf{P}_{k+1|k} = J_f(\hat{\mathbf{x}}_{k|k})\mathbf{P}_{k|k}J_f^T(\hat{\mathbf{x}}_{k|k}) + \mathbf{Q}_k \quad (2.38)$$

$J_f(\hat{\mathbf{x}})$ is the Jacobian of $f(\hat{\mathbf{x}})$.

$$J_f(\hat{\mathbf{x}}_{k|k}) = \begin{pmatrix} 1 & \frac{s}{\omega_{k|k}} & -\frac{1-c}{\omega_{k|k}} & \frac{\omega_{k|k}tc-s}{\omega_{k|k}}\dot{x}_{k|k} - \frac{\omega_{k|k}ts+c-1}{\omega_{k|k}}\dot{y}_{k|k} \\ 0 & c & -s & -ts\dot{x}_{k|k} - tc\dot{y}_{k|k} \\ 0 & s & c & tc\dot{x}_{k|k} - ts\dot{y}_{k|k} \\ 0 & 0 & 0 & 1 \end{pmatrix} \quad (2.39)$$

$$s = \sin(\omega_{k|k}t) \quad (2.40)$$

$$c = \cos(\omega_{k|k}t) \quad (2.41)$$

The a-priori measurement and covariance matrix prediction are given by,

$$\hat{\mathbf{z}}_{k+1|k} = \mathbf{H}\hat{\mathbf{x}}_{k+1|k} \quad (2.42)$$

$$\mathbf{S}_{k+1} = \mathbf{H}\mathbf{P}_{k+1|k}\mathbf{H}^T + \mathbf{R}, \quad (2.43)$$

with \mathbf{R} being the variance of the measurement.

Now the a-posteriori state and covariance can be calculated as follows:

$$\hat{\mathbf{x}}_{k+1|k+1} = \hat{\mathbf{x}}_{k+1|k} + \mathbf{K}_{k+1}(z_{k+1} - \hat{z}_{k+1|k}) \quad (2.44)$$

$$\mathbf{P}_{k+1|k+1} = \mathbf{P}_{k+1|k} - \mathbf{K}_{k+1}\mathbf{S}_{k+1}\mathbf{K}_{k+1}^T \quad (2.45)$$

with \mathbf{K}_{k+1} being the Kalman gain,

$$\mathbf{K}_{k+1} = \mathbf{P}_{k+1|k}\mathbf{H}^T\mathbf{S}_{k+1}^{-1} \quad (2.46)$$

An ahead prediction can be made by evaluating the first component of equation 2.37 with an arbitrary prediction time ΔT .

$$\hat{x}(kt + \Delta T) = \hat{x}_{k|k} + \frac{\sin(\omega_{k|k}t)}{\omega_{k|k}}\hat{x}_{k|k} - \frac{1 - \cos(\omega_{k|k}t)}{\omega_{k|k}}\hat{y}_{k|k} \quad (2.47)$$

2.4 Developed Algorithm

In this section the developed algorithm is discussed in detail.

2.4.1 Armadillo Linear Algebra Library

The algorithm was developed in C++, using a linear algebra library called Armadillo [46]. Armadillo is a high quality C++ linear algebra library, aiming towards a good balance between speed and ease of use. Its syntax is deliberately similar to Matlab and therefore useful for algorithm development, or conversion of research code to C++. It provides classes for 1st-3rd order tensors, overloaded operators for easy use of fundamental operators and more than 200 functions. Armadillo can be used in both open-source and proprietary (closed-source) software.

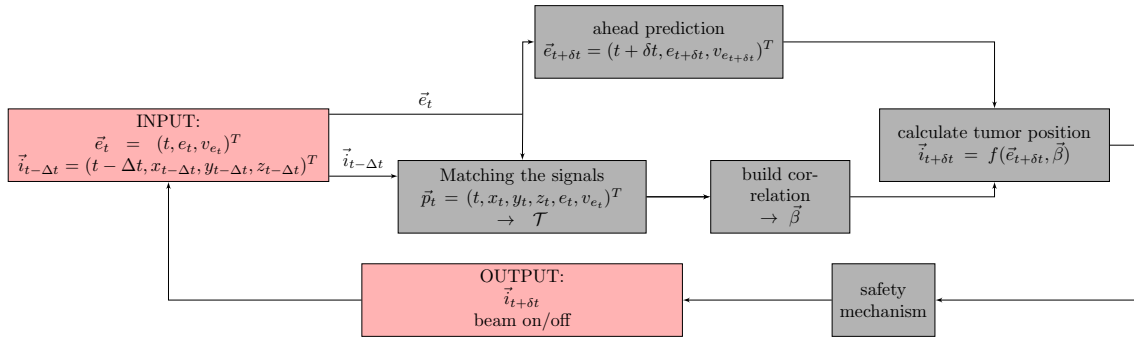


Figure 2.4: Conceptual workflow of the algorithm

2.4.2 Conceptual Workflow

The conceptual workflow of the algorithm is illustrated in figure 2.4. The algorithm works with two inputs: (1) the delayed internal data-points $\vec{i}_{t-\Delta t}$ with Δt being the imaging latency and (2) the external data-points \vec{e}_t . The internal data-points contain the 3D information about the tumor position and a time-stamp of when it was acquired: $\vec{i}_{t-\Delta t} = (t - \Delta t, x_{t-\Delta t}, y_{t-\Delta t}, z_{t-\Delta t})^T$. The external data-points contain 2D information about displacement and velocity of the chest and a time-stamp: $\vec{e}_t = (t, e_t, v_{e_t})^T$. If the external data is multidimensional, principal component analysis has to be performed on the data beforehand for dimensionality reduction.

The algorithm matches the two signals to a paired data point containing the corresponding internal and external information $\vec{p}_t = (t, x_t, y_t, z_t, e_t, v_{e_t})^T$, which are

sorted into the training matrix \mathcal{T} . The training matrix is used to build the correlation function $f(\vec{e}_t, \vec{\beta})$.

The EKF-LCM predictor uses the external data to perform the ahead prediction δt .

The predicted state reads, $\vec{e}_{t+\delta t} = (t + \delta t, e_{t+\delta t}, v_{e_{t+\delta t}})^T$.

The estimated internal position can then be calculated by: $\vec{i}_{t+\delta t}^{est.} = f(\vec{e}_{t+\delta t}, \vec{\beta})$.

In order to avoid undesired radiation during irregular and unpredictable patient behaviour various safety mechanisms are included, which are further discussed in the next section. The algorithm output contains the position estimate and a "beam switch", hence a boolean that controls whether the beam should be turned on or not.

2.4.3 Decision Tree

To better illustrate how the algorithm works, we take a closer look at the decision tree during one iteration. A flowchart of the decision tree is shown in figure 2.6. The iteration can be subdivided into 10 segments, with every segment containing at least one action (blue) or a combination of actions and decision (red). We will now give a more detailed explanation for each segment shown in the flowchart. Some of the segments in figure 2.6 are Cyberknife-specific but can easily be modified to fit the Vero model.

1. *New external data point.* An external motion data point $\vec{e}_t = (t, e_t, v_{e_t})^T$ arrives.
2. *Caching external data.* The external data point is put into a cache

$$\mathbf{C} = \begin{pmatrix} t_i & e_{t_i} & v_{e_{t_i}} \\ t_{i-1} & e_{t_{i-1}} & v_{e_{t_{i-1}}} \\ \vdots & \vdots & \vdots \\ t_{i-n} & e_{t_{i-n}} & v_{e_{t_{i-n}}} \end{pmatrix} \quad (2.48)$$

with a buffer limited to the latest ~ 10 s of external data points, which at a 30 Hz sampling rate corresponds to 300 data points. If this limit is surpassed a first-in-first-out (FIFO) approach is used to update the cache. The timespan that is comprised by the data in the cache has to be larger than the latency of the image acquisition. The reason for this will be made clear in segment 4.

Furthermore, the data has to comprise at least one breathing period (see segment 3.).

3. *Irregular breathing detection.* Using the cached external data, the average over the position is calculated at every newly acquired external point, thereby obtaining the moving average.

$$\mu_i = \frac{1}{n+1} \sum_{j=0}^n e(t_{i-j}) \quad (2.49)$$

The velocity of this moving average can be used to monitor breathing irregularities of the patient. Coughing, yawning or even movement of the patient would result in an offset of the signal and further to an increase in the velocity of the moving average. If the moving average velocity surpasses a certain threshold, treatment is stopped and we wait for the next data-point to be streamed. A reasonable choice of this threshold would be that the moving average must not change more than 3mm in 3s.

4. *Internal data point.* Every time a new external data point $\vec{e}_t = (t, e_t, v_{e_t})^T$ arrives, the algorithm checks if an internal point $\vec{i}_{t_i-\Delta t} = (t_i - \Delta t, x_{t_i-\Delta t}, y_{t_i-\Delta t}, z_{t_i-\Delta t})$ was acquired. If there is no new internal data point, steps 4a to 6 are skipped.

- (a) *Estimation check.* The acquired internal point is compared to the former estimation of this point.

$$|\vec{i}_{t_i-\Delta t} - \vec{i}_{t_i-\Delta t}^{est.}| = \epsilon_i \quad (2.50)$$

If the error ϵ_i surpasses a specified threshold, beam is turned off to wait for new internal data to see if the correlation is broken or if the point is just an outlier. If multiple points in a row are outside the threshold, the correlation is most certainly broken and the model has to be retrained - i.e. the training matrices \mathcal{T} are emptied (see segment 5) and a new training phase starts.

- (b) *Matching.* The time stamp of the internal data-point $\vec{i}_{t_i-\Delta t}$ is compared to the corresponding data point in the cache C . The two signals are matched to a paired data point containing the corresponding internal and external information $\vec{p}_t = (t, x_t, y_t, z_t, e_t, v_{e_t})^T$.

5. *Training.* This segment is method-specific, whereby figure 2.4 shows the Cyberknife method.

Cyberknife: The data point \vec{p} is sorted into an inhalation and an exhalation training matrix (\mathcal{T}_{in} and \mathcal{T}_{ex}) holding a maximum of 20 datapoints (20x6 matrix), again with a FIFO approach. As long as \mathcal{T}_{in} and \mathcal{T}_{ex} are not filled to capacity, we are in the training phase, which means that the beam is switched off because the

correlation has to be built or rebuilt. Only if \mathcal{T}_{in} as well as \mathcal{T}_{ex} contain exactly 20 data points, a third training matrix \mathcal{T}_{lin} , a combination of unique values of \mathcal{T}_{in} and \mathcal{T}_{ex} is created and we proceed to 6.

Vero: All data points are moved into the Vero training matrix \mathcal{T}_{vero} , with a data buffer limited to 30 data points. Again only if \mathcal{T}_{vero} is filled to capacity, we can proceed to 6.

6. *Principal Component Analysis*. PCA is performed on the internal motion of the training matrices. With the rotation matrix \mathbf{R} and the mean vector $\vec{\mu}$ the transformation into principal component space reads,

$$\begin{pmatrix} x_{pca_1} & y_{pca_1} & z_{pca_1} \\ x_{pca_2} & y_{pca_2} & z_{pca_2} \\ \vdots & \vdots & \vdots \\ x_{pca_{20}} & y_{pca_{20}} & z_{pca_{20}} \end{pmatrix} = \left[\begin{pmatrix} x_1 & y_1 & z_1 \\ x_2 & y_2 & z_2 \\ \vdots & \vdots & \vdots \\ x_{20} & y_{20} & z_{20} \end{pmatrix} - \vec{\mu} \right] \cdot \mathbf{R}. \quad (2.51)$$

The PCA rotates the x-axis of the coordinate system into the direction in which the tumor moves predominantly. As shown in figure 2.5 this leaves us with only one significant variable, i.e. the first principal component x_{pca} .

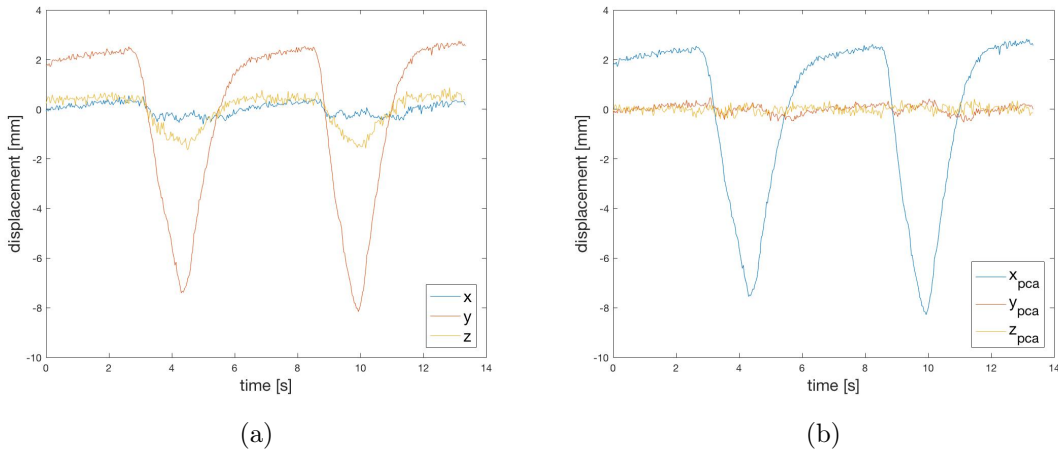


Figure 2.5

- (a) *Correlation check*. The linear correlation coefficient between the 1st principal component x_{pca_i} and the external motion e_{t_i} is calculated and checked whether the correlation surpasses a certain threshold, for instance 90%. If this condition

is not met, there is no point in trying to build a correlation, thus we have to wait for new data points and go back to segment 1.

- (b) *Regression.* This segment is again method-specific, whereby figure 2.4 shows the Cyberknife method.

Cyberknife: The regression coefficients $\vec{\beta}_{in}$, $\vec{\beta}_{ex}$ and $\vec{\beta}_{lin}$ between the 1st principal component x_{pca_i} and the external position e_{t_i} are calculated for all three training matrices. Quadratic regression is used for $\mathcal{T}_{in}/\mathcal{T}_{ex}$, and linear regression for \mathcal{T}_{lin} .

Vero: The regression coefficient $\vec{\beta}_{vero}$ between the 1st principal component x_{pca_i} and the external position e_{t_i} and velocity is calculated for \mathcal{T}_{vero} . Quadratic multivariate regression is used.

7. *Ahead prediction.* The EKF-LCM predictor uses the external data-point $\vec{e}_t = (t, e_t, v_{e_t})^T$ to predict $\vec{e}_{t+\delta t} = (t + \delta t, e_{t+\delta t}, v_{e_{t+\delta t}})^T$.

8. *Evaluation.* The predicted external data is used to evaluate the internal motion with the method specific correlation function $f(\vec{e}_t, \vec{\beta})$.

Cyberknife Evaluate $\vec{x}_{pca}^{est.} = f(e_{t+\delta t}, \vec{\beta}_{in})$, $\vec{x}_{pca}^{est.} = f(e_{t+\delta t}, \vec{\beta}_{ex})$ and $\vec{x}_{pca}^{est.} = f(e_{t+\delta t}, \vec{\beta}_{lin})$ and use blending mechanism as discussed in section 2.1.

Vero Evaluate $\vec{x}_{pca}^{est.} = f(e_{t+\delta t}, v_{e_{t+\delta t}}, \vec{\beta}_{vero})$ as discussed in section 2.2.

9. *Original coordinates.* Note that the the obtained internal estimation $\vec{x}_{pca}^{est.}$ is one dimensional and in principal component space. In this coordinate system $y_{pca}^{est.}$ and $z_{pca}^{est.}$ fluctuate around zero as seen in figure 2.5. Therefore we set $y_{pca}^{est.} = z_{pca}^{est.} = 0$. The back-transformation into the original coordinate system reads,

$$\begin{pmatrix} x_{t+\delta t}^{est.} & y_{t+\delta t}^{est.} & z_{t+\delta t}^{est.} \end{pmatrix} = \begin{pmatrix} x_{pca}^{est.} & 0 & 0 \end{pmatrix} \cdot \mathbf{R} + \vec{\mu} \quad (2.52)$$

10. *Output.* The estimated position of the tumor $\begin{pmatrix} x_{t+\delta t}^{est.} & y_{t+\delta t}^{est.} & z_{t+\delta t}^{est.} \end{pmatrix}$.

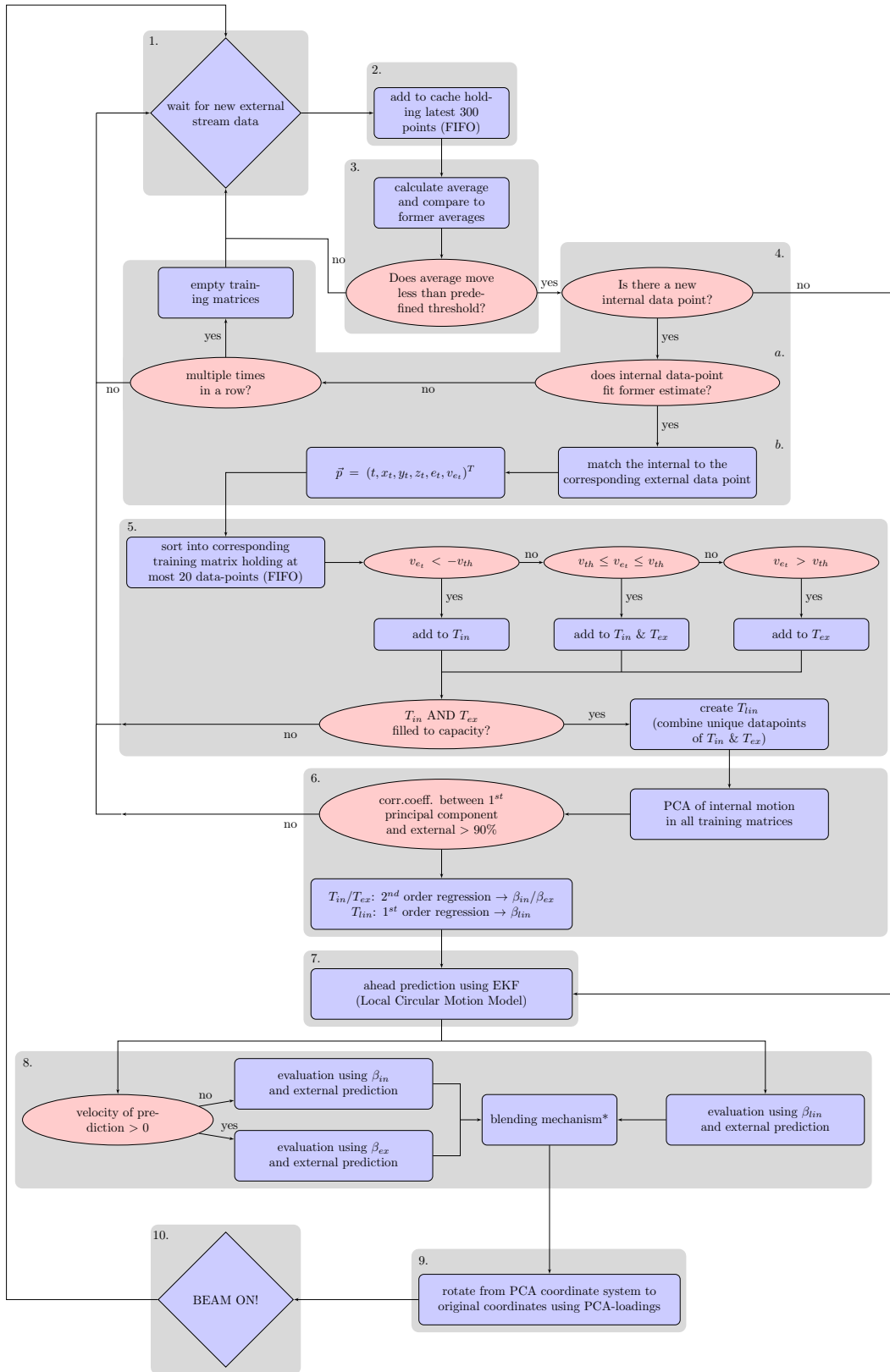


Figure 2.6: Algorithm workflow overview

Chapter 3

Results

In this section the applied methods and the developed algorithm were evaluated on patient data measured on 8 patients. The data was provided courtesy of Yvette Seppenwoolde [44] and was measured at the Mitsubishi RTRT system in Japan in combination with the AZ 733 Anzai medical pressure belt. The data comprises corresponding 3D tumor motion and 1D chest motion, both acquired at a 30Hz sampling rate. The number of traces per patient varied between 2 and 38. The mean signal length and the mean peak-to-peak (p-to-p) displacement per patient is presented in table 3.1.

Patient ID	1	2	3	4	5	6	7	8
Nr. of traces	4	2	2	38	27	28	11	8
P-to-p displ. (mean) [mm]	21.16	15.35	11.3	10.6	10.4	13.1	11.7	19.9
Signal length (mean) [s]	54	73	37	70	110	92	152	120

Table 3.1: Description of the patient data: the data comprises eight patients with varying number of traces, the mean peak-to-peak displacement and the mean signal length

In the first part, the effects of different updating scenarios on the efficiency of correlation models are discussed. We will then discuss the capabilities and limits of the EKF-predictor. In the last part, the performance of the developed algorithm are shown for a realistic choice of the ahead prediction time and the updating frequency.

3.1 Updating efficiency

The 30 Hz Mitsubishi RTRT patient data was simulated for different internal imaging frequencies and for an internal/external latency of 2s. Two updating strategies were employed:

1. *Clinical updating (rebuild)*. Currently used clinically in the Cyberknife®/Synchrony™ system. After the training phase, an internal data point is taken every several seconds to a few minutes. The data point is then compared to the estimation. If the error is larger than a predefined threshold, treatment is stopped to rebuild the correlation during a new training phase.
2. *Automated updating*. Improving the correlation dynamically by utilizing an update sample rate that is comparable to the training sample rate. The training data is updated after each of the imaging data is acquired by using a first-in-first-out (FIFO) approach.

The initial correlation was built with a 2Hz internal sampling frequency in all cases. The correlation was then updated every 0.5s to 60s. Below 5s automated updating was used, above 5s clinical updating was used.

Figure 3.1 shows the average root-mean-squared error (RMSE) over all patients for different updating intervals for both the Cyberknife- and the vero4DRT method.

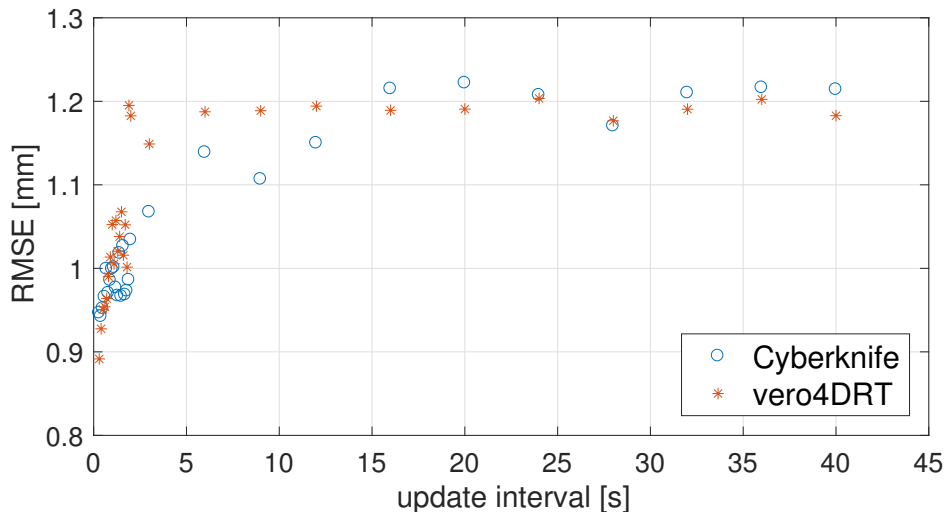


Figure 3.1: RMSE between estimate and real signal for different updating intervals (average taken over all traces)

3.2 Prediction Potentials and Limits

The EKF-LCM predictor was implemented as described in section 2.3. The parameters q_1 , q_2 and q_3 were set to 0.2, $2 \cdot 10^{-4}$ and $2 \cdot 10^{-3}$, respectively as proposed in [39]. The measurement variance R is setup specific. The AZ 733 Anzai medical belt has a signal to noise ratio of $\sim 28dB$ [47]. For a 10mm amplitude this results in $R \sim 0.01$. The EKF-LCM predictor was evaluated using the external signal. Four different sampling frequencies (30Hz, 15Hz, 10Hz and 5Hz) were simulated with four latencies (100ms-400ms). Figure 3.2 shows the average RMSE over all traces for all sampling frequencies and prediction intervals. The predictor shows to be extremely robust against varying sampling frequencies.

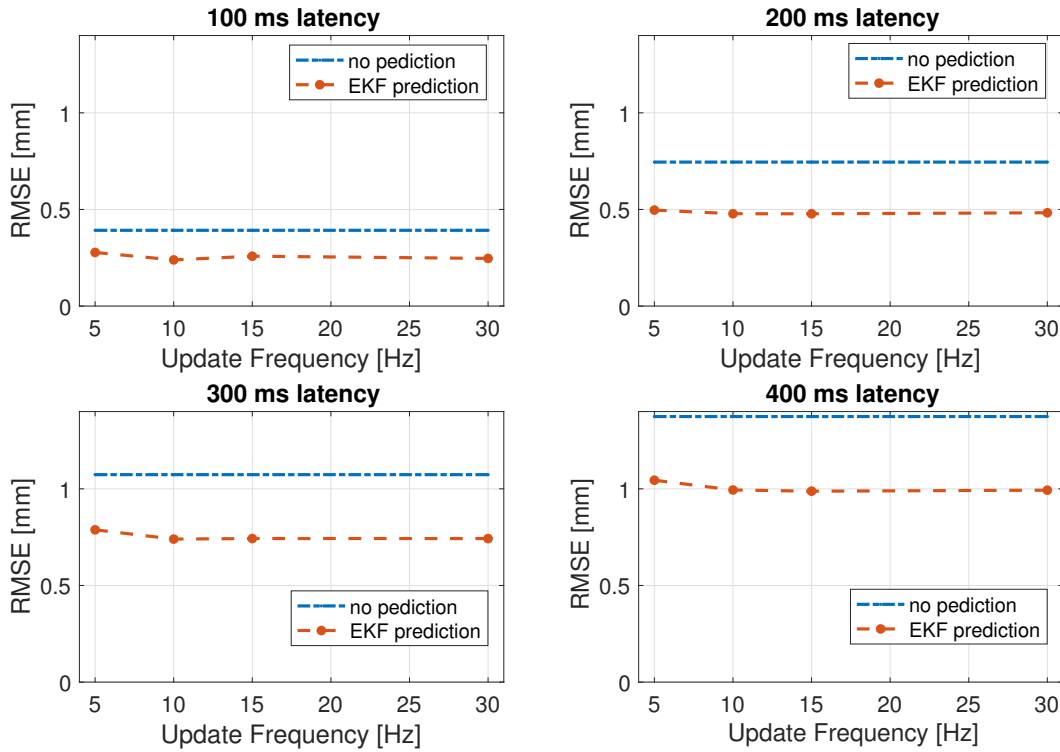


Figure 3.2: Average RMSE over all traces with and without prediction: sampling frequencies (5Hz-30Hz) and latencies (100ms-400ms)

Fig. 3.3 and 3.4 illustrate the breakdown of the EKF-LCM for high ahead prediction intervals. They show the prediction traces (red) and the measurement traces (blue) for different prediction intervals on a single patient, showing a large variation in the breathing amplitude.

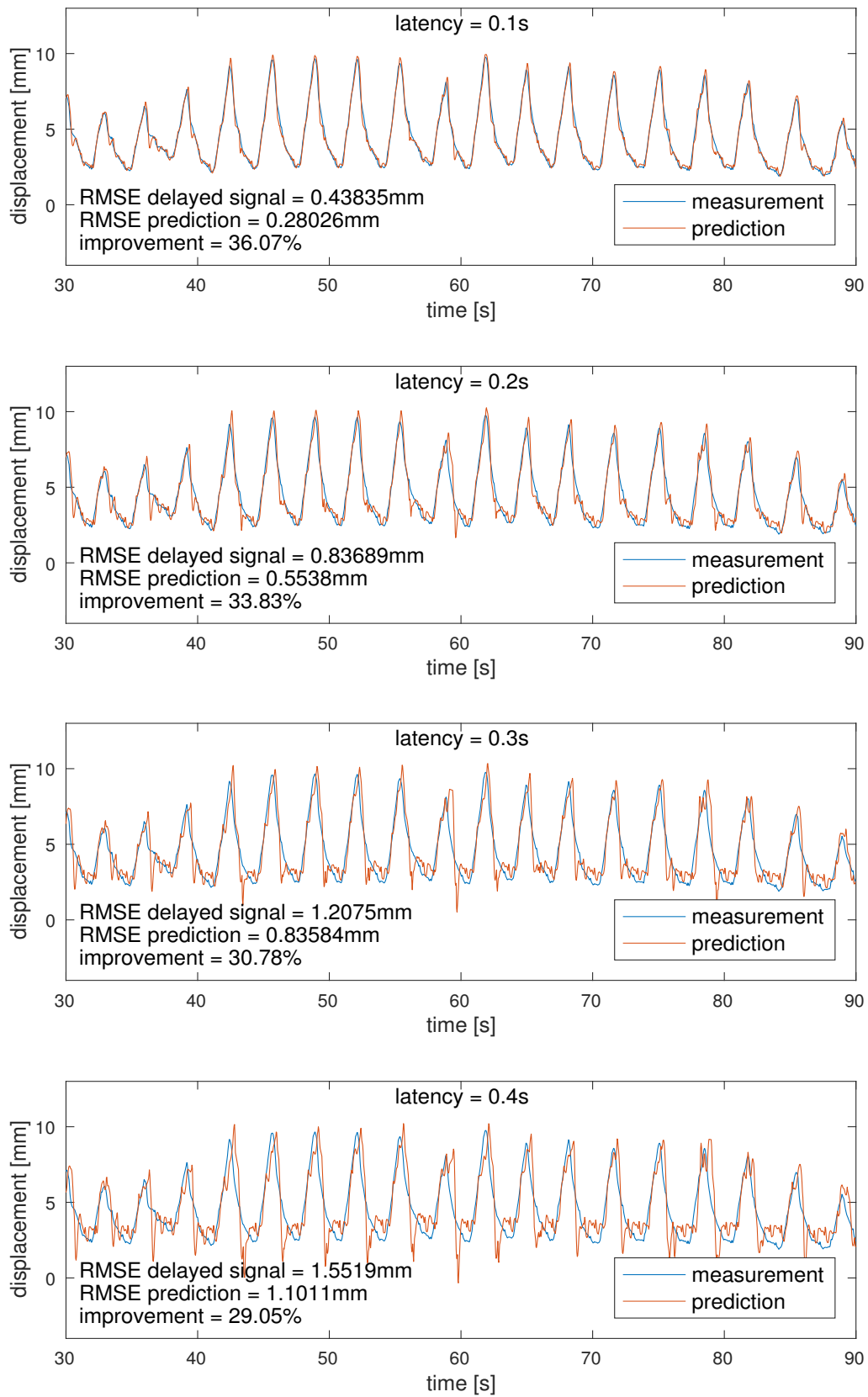


Figure 3.3: LCM-prediction for different prediction intervals (0.1 – 0.4s)

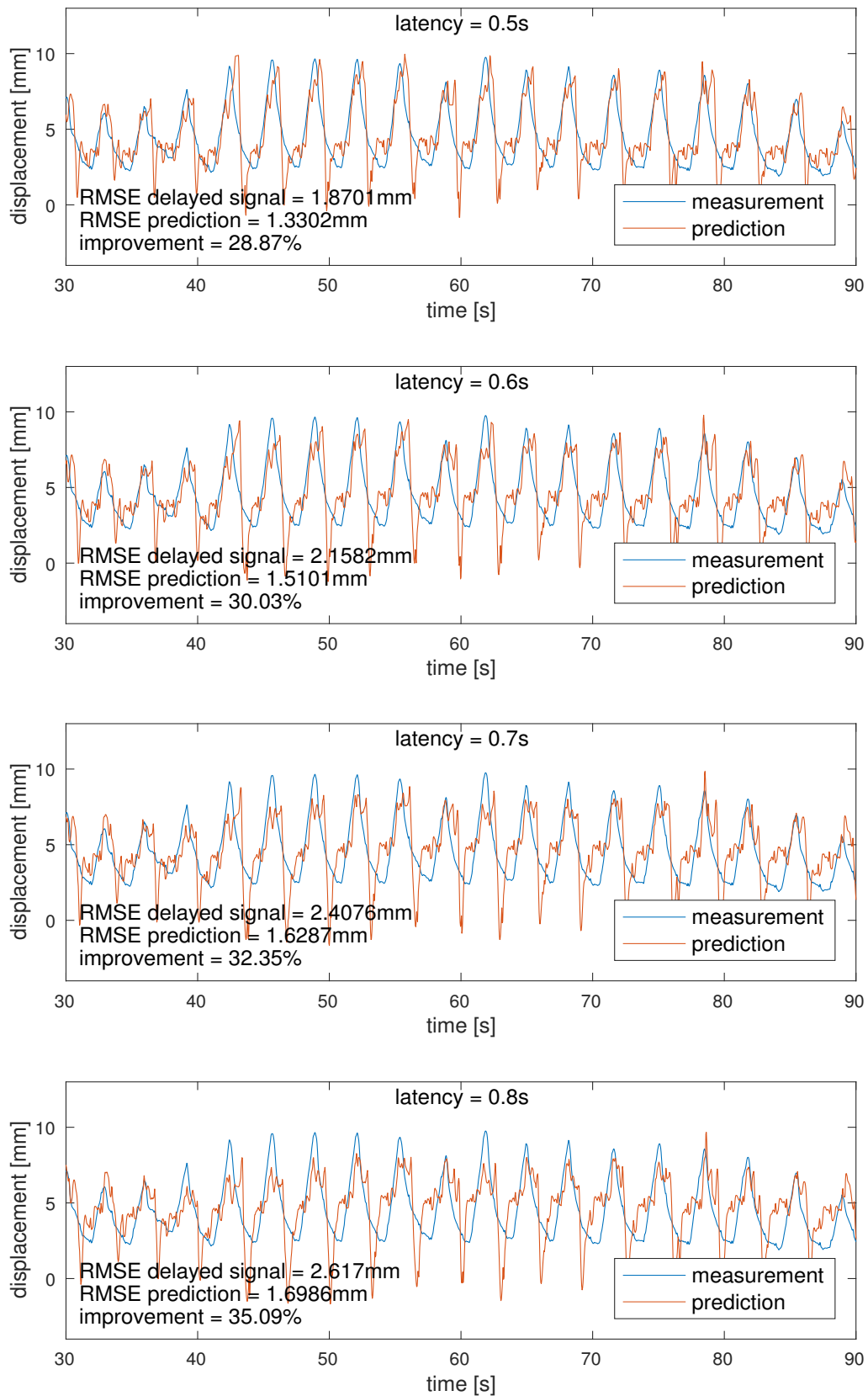


Figure 3.4: LCM-prediction for different prediction intervals (0.5 – 0.8s)

3.3 Algorithm Performance

The performance of the developed algorithm was simulated for a realistic choice of parameters, in order to evaluate its precision. The latency was set to be 2s. The internal imaging frequency during training was set to 2Hz with a 2Hz updating frequency. The ahead prediction was set to 100ms.

Table 3.2 shows the mean RMSE in three dimensions for both the Cyberknife and the Vero method. Patient 3 was not evaluated, because the signal length is too short ($\sim 30s$) to get meaningful results.

Patient ID	1	2	4	5	6	7	8
Nr. of traces	4	2	38	27	28	11	8
P-to-p displ. (mean) [mm]	21.16	15.35	10.6	10.4	13.1	11.7	19.9
Signal length (mean) [s]	54	73	70	110	92	152	120
Cyberknife mean RMSE [mm]	1.53	1.42	1.51	1.18	0.93	0.93	1.65
Vero4DRT mean RMSE [mm]	1.52	1.41	1.23	1.20	0.93	0.88	1.64

Table 3.2: Patient data evaluation using the developed algorithm showing:

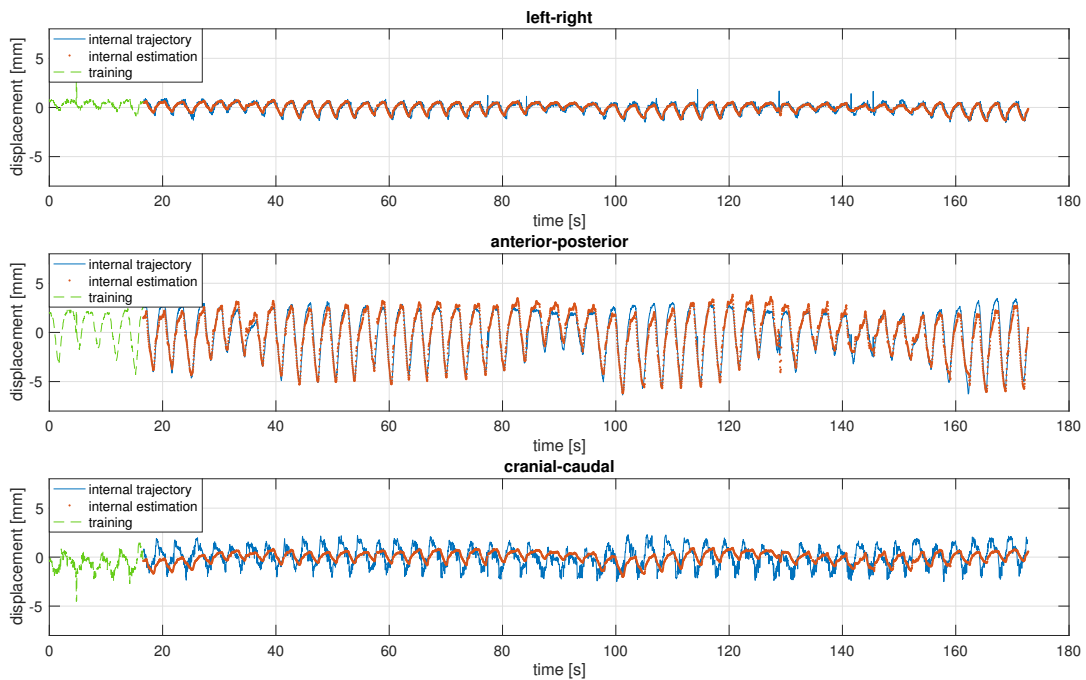


Figure 3.5: Estimation trajectories using the developed algorithm (RMSE=1.18mm)

Due to the choice of the predictor as an EKF, the algorithm stands out through its speed. The average estimation time of one data point is less than 0.2ms.

Figure 3.5 presents one of the traces of patient 5 and the corresponding estimated trajectories using the developed algorithm. The RMSE in this case is 1.18mm. This should give an idea about the precision of the estimation. The first $\sim 20s$ are used for training. The estimated trajectory is shown for all body axes (left-right, anterior-posterior and caudal-cranial).

Chapter 4

Discussion and Conclusion

In this thesis we proposed a new algorithm that combines prediction and correlations methods for compensating large system latencies. Correlation models are used to build a correlation between 1D external surrogates and 3D internal target motion. The EKF-LCM predictor is used to predict the external 1D surrogate motion. This prediction is in turn used to estimate the future tumor position.

Two correlation models were implemented in the algorithm, used in the Cyberknife and the vero4DRT system. We could show that fast, automated updating of the correlation function can lead to $\sim 25\%$ reduction in the RMSE. Updating intervals below 2s show the best results. For updating times above 5s the mean RMSE over all patients plateaus and stays constant (fig. 3.1). Updating intervals between 2s and 6s should not be used, because the period of a breathing cycle is also within this range. This may lead to a lack of diversity in the training data, as all data-points come from a similar breathing phase. The training data is therefore no longer representative of the entire breathing cycle.

In terms of accuracy, no significant difference was determined between the two models. However, the Cyberknife model requires a predefined overlap parameter σ for the blending mechanism between the inhalation- and exhalation correlation function (see section 2.1). The vero4DRT model does not rely on predefined parameters.

The EKF-LCM predictor performs well up until $\sim 400ms$, but breaks down for higher prediction intervals as shown in figure 3.3 and 3.4. This is because the assumption of a local circular motion fails for larger times. Additionally, the model uses a first order EKF, which linearises the equations of motion, making it

unsuitable for predicting large time intervals. The performance of the EKF-LCM predictor is almost the same for different and varying sampling frequencies. The improvement that was achieved by the predictor compared to no prediction at all was $\sim 30\%$.

The algorithm was developed to deal with 1D external surrogate data. The external data acquisition is not limited to a strain belt, as it was used in this project. Other surrogates such as spirometry or infra-red markers can also be used. Higher dimensional surrogate signals, such as multiple infra-red markers, can be used to find the most significant component e.g. by making use of PCA.

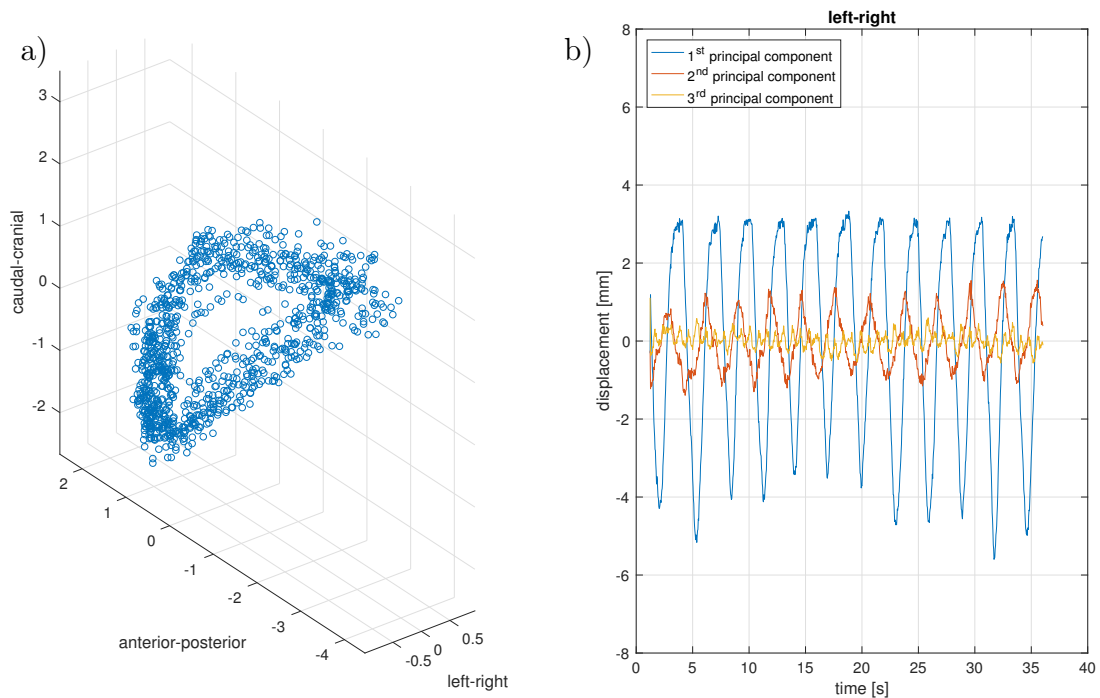


Figure 4.1: Tumor motion: a) 3D scatter plot of circular tumor motion b) temporal tumor movement in principal component space

The correlation function is built using the first principle component of the internal movement, hence the direction of largest displacement. This leads to limitations in case of tumor paths that move circularly such as shown in figure 4.1a. A circular tumor motion leads to a non-zero second principal component with a phase shift. This is illustrated in figure 4.1b, showing the principal components of the tumor

displacement. The second principal component shows a phase shifted semi-periodic motion. The third principal component is again fluctuating around zero and shows no predictable pattern. The movement of the second principle component is ignored in the developed algorithm and can lead to slightly higher errors for patients in which the tumor moves in a circular path. In our case, patients 1,4,5 and 8 show a high circular tumor motion. Therefore they show a slightly higher RMSE ranging from 1.2-1.64mm as shown in table 3.2. Patient 6 and 7, who show virtually no circular movement, have an RMSE of below 1mm (see table 3.2).

As an extension of this thesis, it would be interesting to find a way to compensate this circular tumor motion. This would require an external signal that is well correlated to the phase shifted component. Another way would be to find the time lag between the two signals using their cross-correlation. The correlation could be built using the time-lagged surrogate signal and the phase-shifted second principal component.

Another issue of tumor motion relates to the potential of rotation and deformation during the breathing cycle. Wu et al. [48] examined the rotation and deformation of lung tumors with respect to the motion in 3D in 30 patients. They used the GTV contour from end-inhale and mapped it to end-exhale. The results were evaluated using the overlap index, which is a measure of similarity. Three scenarios were evaluated: (1) translation only (2) translation + rotation and (3) translation + rotation + deformation. The overlap index increases after translation + rotation and translation + rotation + deformation compared to translation only were 1.1% and 1.4% respectively. Moreover, the results did not depend on GTV size and respiratory motion amplitude. The study showed that the primary effect of normal respiration on lung tumors was translation. Rotation and deformation of lung tumors were determined to be negligible.

This MSc project aimed to compensate the latency for systems that show an extremely high latency of more than 2s. However, this high latency is system- and problem specific and can be avoided. Poulsen et al. [49] showed that the image acquisition and file writing for MV and kV images of the PortalVision AS1000 portal imager system and a kV On-Board Imager system (Varian Medical Systems) takes $\sim 300ms$. Furtado et al. [50] used paired mega-voltage and kilo-voltage images

for 2D/3D registration with a mean registration time of 188ms. In the case of dynamic MLC tracking, where the MLC leaves are repositioned dynamically instead of the LINAC, Poulsen et al. [49] measured 16ms for MLC position calculation and 52ms for MLC adjustment. This leaves an overall latency of less than 600ms that needs to be compensated, a major part of which is used for image acquisition and file writing. Further reductions of the latency to below 400ms could open the door for real time tumor tracking that does not rely on external surrogates. The EKF-LCM predictor, due to its near-constant accuracy for low imaging frequency would present a reasonable choice.

However, at the present time we could show that for systems with higher latencies the use of combined correlation and prediction can lead to good results.

Acknowledgments

I would like to thank all the people who have supported and accompanied me throughout the project. I especially want to thank:

- *Univ.-Prof. Dr. DI Dietmar Georg* for giving me the chance to work on this project and making it my master thesis at AKH, Vienna.
- *Hugo Furtado, MSc PhD*: for introducing me to the world of medical physics and technology and for running this project together with me. Thanks to his interdisciplinary skills, he was always able to help me find solutions to problems that opened up.

Lastly, I would like to thank my family, my friends and my girlfriend Clara, who have supported me throughout my studies.

Bibliography

- [1] Statistik Austria. Cancer incidence. http://www.statistik.at/web_en/statistics/PeopleSociety/health/cancer_incidence/index.html.
- [2] H. Pfeifer. Experimentalphysik 3, Atome, Moleküle und Festkörper. *Zeitschrift für Physikalische Chemie*, 200(Part_1_2):278–279, 1997.
- [3] ICRU. *ICRU Report 50: Prescribing, Recording, and Reporting Photon Beam Therapy*. 1993.
- [4] International Commission on Radiation Units and Measurements. ICRU Report 62. Prescribing, Recording, and Reporting Photon Beam Therapy (Supplement to ICRU Report 50). *Journal of ICRU*, (November):Ix +52, 1999.
- [5] E. B. Podgorsak and Kristofer Kainz. Radiation Oncology Physics: A Handbook for Teachers and Students. *Medical Physics*, 33(6):1920, 2006.
- [6] ICRU. ICRU Report 78: Prescribing, Recording and Reporting Proton-Beam Therapy. In *Journal of the ICRU*, volume 7, pages 131–134. 2008.
- [7] N. Hodapp. The ICRU Report No. 83: Prescribing, recording and reporting photon-beam intensity-modulated radiation therapy (IMRT), 2012.
- [8] Niko Papanikolaou. Handbook of Radiotherapy Physics: Theory and Practice. *Medical Physics*, 35(9):4281–4281, 2008.
- [9] Dietmar Georg Basic Seminar of Radiation Oncology Physics 2017.
- [10] Di Yan. *Image-Guided/Adaptive Radiotherapy*, pages 321–336. Springer Berlin Heidelberg, Berlin, Heidelberg, 2006.
- [11] Paul J. Keall, Gig S. Mageras, James M. Balter, Richard S. Emery, Kenneth M. Forster, Steve B. Jiang, Jeffrey M. Kapatoes, Daniel A. Low, Martin J. Murphy,

- Brad R. Murray, Chester R. Ramsey, Marcel B. Van Herk, S. Sastry Vedam, John W. Wong, and Ellen Yorke. The management of respiratory motion in radiation oncology report of AAPM Task Group 76, 2006.
- [12] Statistik Austria. Cancer survival. http://www.statistik.at/web_en/statistics/PeopleSociety/health/cancer_incidence/cancer_survival/index.html.
- [13] M Machtay, S Swann, R Komaki, R Byhardt, R Paulus, W Sause, K Albain, B Movsas, and W J Curran. Higher BED is Associated with Improved Local-regional Control and Survival for NSCLC Treated with Chemoradiotherapy: An RTOG Analysis. *Int J Radiat Oncol Biol Phys.*, 63(2):S40, 2005.
- [14] Stefan L.S. Kwa, Joos V. Lebesque, Jacqueline C.M. Theuws, Lawrence B. Marks, Mike T. Munley, Gunilla Bentel, Dieter Oetzel, Uwe Spahn, Mary V. Graham, Robert E. Drzymala, James A. Purdy, Allen S. Lichter, Mary K. Martel, and Randall K. Ten Haken. Radiation pneumonitis as a function of mean lung dose: An analysis of pooled data of 540 patients. *International Journal of Radiation Oncology Biology Physics*, 42(1):1–9, 1998.
- [15] Ingmar Lax, Henric Blomgren, Ingemar Näslund, and Rut Svanström. Stereotactic radiotherapy of malignancies in the abdomen: Methodological aspects. *Acta Oncologica*, 33(6):677–683, 1994.
- [16] Yoshiharu Negoro, Yasushi Nagata, Tetsuya Aoki, Takashi Mizowaki, Norio Araki, Kenji Takayama, Masaki Kokubo, Shinsuke Yano, Sachiko Koga, Keisuke Sasai, Yuta Shibamoto, and Masahiro Hiraoka. The effectiveness of an immobilization device in conformal radiotherapy for lung tumor: Reduction of respiratory tumor movement and evaluation of the daily setup accuracy. *International Journal of Radiation Oncology Biology Physics*, 50(4):889–898, 2001.
- [17] K. R. Jones. A respiration monitor for use with CT body scanning and other imaging techniques. *British Journal of Radiology*, 55(655):530–533, 1982.
- [18] Kiyoshi Ohara, Toshiyuki Okumura, Masayoshi Akisada, Tetsuo Inada, Takehiko Mori, Hiroshi Yokota, and Mirriam J.B. Calaguas. Irradiation synchronized with respiration gate. *International Journal of Radiation Oncology, Biology, Physics*, 17(4):853–857, 1989.

- [19] Hiroki Shirato, Shinichi Shimizu, Tatsuya Kunieda, Kei Kitamura, Marcel Van Herk, Kenji Kagei, Takeshi Nishioka, Seiko Hashimoto, Katsuhisa Fujita, Hidefumi Aoyama, Kazuhiko Tsuchiya, Kohsuke Kudo, and Kazuo Miyasaka. Physical aspects of a real-time tumor-tracking system for gated radiotherapy. *International Journal of Radiation Oncology Biology Physics*, 48(4):1187–1195, 2000.
- [20] Harold C. Urschel, John J. Kresl, James D. Luketich, Lech Papiez, Robert D. Timmerman, and Raymond A. Schulz. *Treating tumors that move with respiration*. 2007.
- [21] Edward J. Ciaccio. Informationapplied medical image processing: A basic course, by wolfgang birkfellner, associate professor, department of medical physics and biomedical engineering, medical university of vienna, austria. *BioMedical Engineering OnLine*, 10(1):16, Feb 2011.
- [22] Cihat Ozhasoglu and Martin J. Murphy. Issues in respiratory motion compensation during external-beam radiotherapy. *International Journal of Radiation Oncology Biology Physics*, 52(5):1389–1399, 2002.
- [23] S. S. Vedam, V. R. Kini, P. J. Keall, V. Ramakrishnan, H. Mostafavi, and R. Mohan. Quantifying the predictability of diaphragm motion during respiration with a noninvasive external marker. *Medical Physics*, 30(4):505–513, 2003.
- [24] Steve B. Jiang. Technical aspects of image-guided respiration-gated radiation therapy. *Medical Dosimetry*, 31(2):141–151, 2006.
- [25] Synchrony Tracking Vest. Accuracy. <http://accurayorders.com/synchrony-tracking-vest-5-pack-large.html>.
- [26] Deutsches Cyberknife Zentrum. Das cyberknife-system. <http://www.deutsches-cyberknife-zentrum.de/de/cyberknife/index.php>.
- [27] Mitsubishi Heavy Industries Technical Review Vol. 49 No. 1 (March 2012).
- [28] James M. Balter, J. Nelson Wright, Laurence J. Newell, Barry Friemel, Steven Dimmer, Yuki Cheng, John Wong, Edward Vertatschitsch, and Timothy P. Mate. Accuracy of a wireless localization system for radiotherapy. *International Journal of Radiation Oncology Biology Physics*, 61(3):933–937, 2005.

- [29] C. Silva, D. Mateus, M. Eiras, and S. Vieira. Calypso® 4D Localization System: A review, 2013.
- [30] Jan J W Lagendijk, Bas W. Raaymakers, Alexander J E Raaijmakers, Johan Overweg, Kevin J. Brown, Ellen M. Kerkhof, Richard W. van der Put, Björn Hårdemark, Marco van Vulpen, and Uulke A. van der Heide. MRI/linac integration. *Radiotherapy and Oncology*, 86(1):25–29, 2008.
- [31] Calypso Extracranial Tracking. <https://www.varian.com/oncology/products/real-time-tracking-motion-management/calypso-extracranial-tracking>.
- [32] Sjoerd Crijns and Bas Raaymakers. From static to dynamic 1.5T MRI-linac prototype: Impact of gantry position related magnetic field variation on image fidelity. *Physics in Medicine and Biology*, 59(13):3241–3247, 2014.
- [33] A. Hsu, N. R. Miller, P. M. Evans, J. C. Bamber, and S. Webb. Feasibility of using ultrasound for real-time tracking during radiotherapy. In *Medical Physics*, volume 32, pages 1500–1512, 2005.
- [34] A. Schweikard, G. Glosser, M. Bodduluri, M. J. Murphy, and J. R. Adler. Robotic motion compensation for respiratory movement during radiosurgery. *Computer Aided Surgery*, 5(4):263–277, 2000.
- [35] Robert Durichen, Lucas Davenport, Ralf Bruder, Tobias Wissel, Achim Schweikard, and Floris Ernst. Evaluation of the potential of multi-modal sensors for respiratory motion prediction and correlation. In *Proceedings of the Annual International Conference of the IEEE Engineering in Medicine and Biology Society, EMBS*, pages 5678–5681, 2013.
- [36] Ahmad Esmaili Torshabi, Andrea Pella, Marco Riboldi, and Guido Baroni. Targeting accuracy in real-time tumor tracking via external surrogates: A comparative study. *Technology in Cancer Research and Treatment*, 9(6):551–561, 2010.
- [37] S. S. Vedam, P. J. Keall, A. Docef, D. A. Todor, V. R. Kini, and R. Mohan. Predicting respiratory motion for four-dimensional radiotherapy. *Medical Physics*, 31(8):2274–2283, 2004.

- [38] L Ramrath, A Schlaefer, F Ernst, S Dieterich, and A Schweikard. Prediction of respiratory motion with a multi-frequency based Extended Kalman Filter. *IJCARS*, 2:56–58, 2007.
- [39] S. M. Hong, B. H. Jung, and D. Ruan. Real-time prediction of respiratory motion based on a local dynamic model in an augmented space. *Physics in Medicine and Biology*, 56(6):1775–1789, 2011.
- [40] Nadeem Riaz, Piyush Shanker, Rodney Wiersma, Olafur Gudmundsson, Weihua Mao, Bernard Widrow, and Lei Xing. Predicting respiratory tumor motion with multi-dimensional adaptive filters and support vector regression. *Physics in Medicine and Biology*, 54(19):5735–5748, 2009.
- [41] Floris Ernst, Alexander Schlaefer, Sonja Dieterich, and Achim Schweikard. A Fast Lane Approach to LMS prediction of respiratory motion signals. *Biomedical Signal Processing and Control*, 3(4):291–299, 2008.
- [42] Gregory C. Sharp, Steve B. Jiang, Shinichi Shimizu, and Hiroki Shirato. Prediction of respiratory tumour motion for real-time image-guided radiotherapy. *Physics in Medicine and Biology*, 49(3):425–440, 2004.
- [43] Floris Ernst, Ralf Bruder, Alexander Schlaefer, and Achim Schweikard. Correlation between external and internal respiratory motion: A validation study. *International Journal of Computer Assisted Radiology and Surgery*, 7(3):483–492, 2012.
- [44] Yvette Seppenwoolde, Hiroki Shirato, Kei Kitamura, Shinichi Shimizu, Marcel van Herk, Joos V Lebesque, and Kazuo Miyasaka. Precise and real-time measurement of 3D tumor motion in lung due to breathing and heartbeat, measured during radiotherapy. *International Journal of Radiation Oncology - Biology - Physics*, 53(4):822–834, mar 2018.
- [45] Kenneth Poels, Jennifer Dhont, Dirk Verellen, Oliver Blanck, Floris Ernst, Jef Vandemeulebroucke, Tom Depuydt, Guy Storme, and Mark De Ridder. A comparison of two clinical correlation models used for real-time tumor tracking of semi-periodic motion: A focus on geometrical accuracy in lung and liver cancer patients. *Radiotherapy and Oncology*, 115(3):419–424, 2015.
- [46] Conrad Sanderson and Ryan Curtin. Armadillo: a template-based C++ library for linear algebra. *The Journal of Open Source Software*, 1(2), 2016.

- [47] Christian Heinz, Michael Reiner, Claus Belka, Franziska Walter, and Matthias Söhn. Technical evaluation of different respiratory monitoring systems used for 4D CT acquisition under free breathing. *Journal of Applied Clinical Medical Physics*, 16(2):334–349, 2015.
- [48] J. Wu, R. Shekhar, and W. D’souza. TU?FF?A3?03: Do Mobile Tumors in the Lung Deform During Normal Respiration ? An Image Registration Investigation? *Medical Physics*, 34(6):2573, 2007.
- [49] Per Rugaard Poulsen, Byungchul Cho, Amit Sawant, Dan Ruan, and Paul J. Keall. Detailed analysis of latencies in image-based dynamic MLC racking. *Medical Physics*, 37(9):4998–5005, 2010.
- [50] Hugo Furtado, Elisabeth Steiner, Markus Stock, Dietmar Georg, and Wolfgang Birkfellner. Real-time 2d/3d registration using kv-mv image pairs for tumor motion tracking in image guided radiotherapy. *Acta Oncologica*, 52(7):1464–1471, 2013. PMID: 23879647.